Determining domain orientation in macromolecules by using spin-relaxation and residual dipolar coupling measurements

David Fushman*, Ranjani Varadan, Michael Assfalg, Olivier Walker

Department of Chemistry and Biochemistry, Center for Biomolecular Structure and Organization, University of Maryland, 1115 Agriculture/Life Science Surge Bldg (#296), College Park, MD 20742-3360 USA

Contents

* Corresponding author. Tel.: +1-301-405-3461; fax: +1-301-314-0386.
   E-mail address: fushman@umd.edu (D. Fushman).

1. Introduction

Many proteins in the cell have modular architecture, i.e. they are composed of several well-folded regions (domains). Interdomain orientation and dynamics often play an essential role in regulation of functional activity of these systems [1]. Structure characterization of multidomain proteins and protein complexes is therefore of significant interest for the understanding of the mechanisms of regulation of their biological function. However, inherent flexibility of these systems presents a significant challenge to the conventional high-resolution methods for biomolecular structure determination. Crystal packing forces, comparable with weak interactions between the domains, could affect the interdomain orientation and position, so that the conformations observed in protein crystals might represent a snapshot rather than the physiologically relevant conformation in solution. Interdomain distance constraints available from NMR measurements could be limited because of the insufficient number of short-range inter-proton contacts (NOEs) between the domains. Moreover, these $^1H-^1H$ distances are further averaged by interdomain dynamics, which could make the already scarce NOE-derived information uninterpretable. In this situation, long-range, orientational constraints and interface mapping by chemical shift perturbations become indispensable as the source of information about the structure/conformation of multidomain systems.

Recently, NMR approaches have been developed that provide information on molecular orientations. One such approach is based on the anisotropy of the overall rotational diffusion of a molecule that manifests itself in the orientational dependence of spin-relaxation parameters [2–4]. Another approach uses residual dipolar couplings (RDCs) observed due to anisotropy of the distribution of molecular orientations in solution [5,6]. The two methods are based on physically different phenomena and could provide complementary information on molecular structure. There is a growing number of applications of these methods to domain orientations in proteins, some examples can be found in Refs. [2,7–15]. Here we illustrate these approaches by showing how they can be used to determine the domain orientation of a K48-linked di-ubiquitin (Ub$_2$) as a function of pH conditions.

An increasing number of cellular processes have been found to be regulated by ubiquitin-mediated signaling events [16,17], when a specific lysine residue on the surface of the substrate protein is covalently attached to the C-terminus of ubiquitin [18]. Chains of ubiquitin (Ub) are assembled on the substrate via formation of an isopeptide bond between a lysine on the surface of the first Ub and the C-terminal glycine (G76) of the next. The most well characterized is polyubiquitination via K48: these chains are the principal signal for targeting substrates to the proteasome for degradation [19,20], and the tetra-Ub (Ub$_4$) chain was shown to be the minimal signal for efficient proteasomal targeting [21]. Crystallographic approaches so far have resulted in a structure of Ub$_2$ [22] and two structures of Ub$_4$ [23,24], all of them being different from each other. This suggests that the chains are intrinsically flexible, and their conformation in crystals could represent particular snapshots selected by packing forces. NMR studies could, therefore, shed light onto the physiologically relevant conformations of polyUb chains in solution.

Our comparison of amide chemical shifts in Ub$_2$ versus monoUb [13] revealed no specific interaction between Ub domains at acidic conditions (pH 4.5), in contrast with the crystal structure obtained at the same pH [22]. However, at higher pH values we observed consistent differences in chemical shifts between Ub$_2$ and monoUb for those residues clustered in and around the hydrophobic patch comprising L8, I44, and V70 in both Ub domains (Fig. 1). These site-specific perturbations indicated the formation of a hydrophobic interface between the two domains, generally consistent with the one observed in Ub$_2$ crystals at lower pH [22]. Our pH titration data [13] indicate that the interdomain interface in Ub$_2$ in solution is well defined at pH 6.8 and higher; the chemical shift perturbations for most amides saturate at or above pH 7.5 (Fig. 1e). These findings suggest a pH-dependent switch in the Ub$_2$ conformation, from an open one at pH 4.5 to a closed conformation at alkaline pH. Assuming that the chemical shift positions observed at intermediate pH values result from fast equilibrium exchange between open and closed conformations of Ub$_2$, the relative population of the closed conformation at pH 6.8 was estimated to be about 85% [13]. A similar pH-dependent behavior is present in Ub$_4$. The pH-dependent switch model derived from chemical shift data can be characterized in structural terms by applying domain orientation methods to analyze the solution conformations of Ub$_2$.

2. Orienting individual domains in a molecule

2.1. General concept

The general concept of determining interdomain orientation using measurements of the rotational diffusion or alignment tensors is outlined in Fig. 2. The underlying idea is that individual domains tumble or orient together, as a single molecule rather than as independent 'beads on a string'. This could be a result of specific interactions between the domains (e.g. Ub$_2$ at pH 6.8, see below) or could be caused by steric restrictions due to short or relatively rigid interdomain linker (e.g. Abl SH(32) [7] or Ub$_2$ at pH 4.5). The corresponding domain aligning procedure includes the following steps (Fig. 2). First, the orientation of the principal axes frame (PAF) of the tensor of interest is determined for each individual domain using
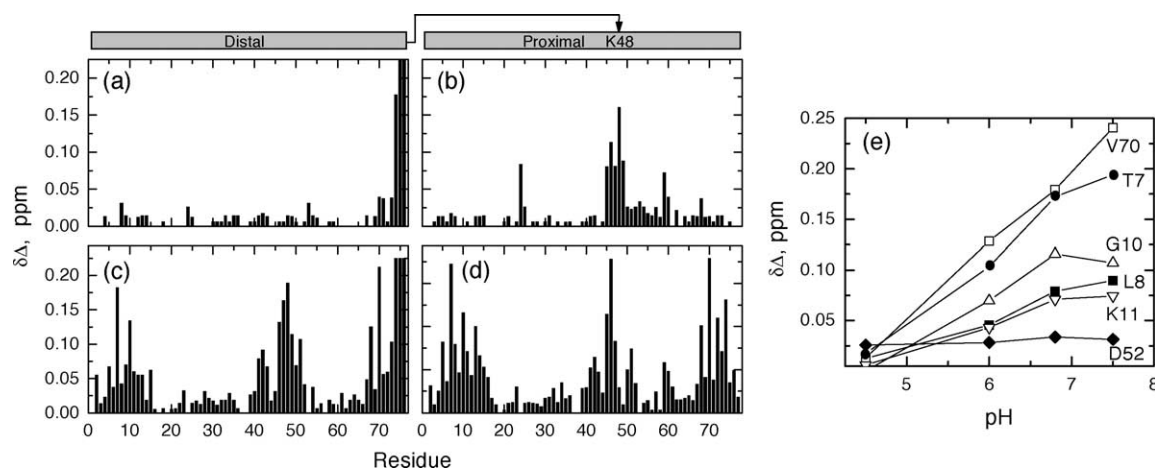
Fig. 1. Chemical shift perturbation data for NH groups indicate a pH-dependent switch in the solution conformation of K48-linked Ub$_2$. Shown are combined amide chemical shift perturbations $\Delta\delta$ (Ub$_2$ versus monoUb) for (a,b) pH 4.5 and (c,d) pH 6.8 and (e) chemical shift perturbations as a function of pH for selected residues. The $\Delta\delta$ values were calculated as $\Delta\delta = [(\Delta\delta_H)^2 + (\Delta\delta_N/5)^2]^{1/2}$, where $\Delta\delta_H$ and $\Delta\delta_N$ are the chemical shift differences between Ub$_2$ and monoUb for ^{1}H and ^{15}N, respectively. Panels (a) and (c) correspond to the distal domain and (b) and (d) to the proximal domain in Ub$_2$, their linkage is schematically shown on the top.

relaxation (diffusion tensor) or RDCs (order tensor) measurements for the whole molecule (see below). This orientation is generally characterized by three Euler angles $\{\alpha, \beta, \gamma\}$ that define the PAF with respect to the atom coordinate (PDB) frame for a given domain. Since the domains reorient together as a single entity, these individual PAFs represent properties of the whole molecule, experienced by each individual domain. Therefore, as a second step, these PAFs determined for the individual domains are aligned such that their corresponding axes

become parallel to each other. Because each PAF is rigidly attached to the coordinate frame of the corresponding domain, this process will result in a proper orientation of the domains with respect to each other.

This approach assumes that the three-dimensional structures of the individual domains are available. Domain structures in the monomeric state can be used for domain alignment purposes, provided these are not perturbed when the multidomain system is formed. It is important to mention that the approach described here provides a time-averaged

Fig. 2. Illustration of the concept of determining interdomain orientation in a multidomain system based on axes orientation for diffusion or alignment tensors of the molecule experienced by each of the domains.

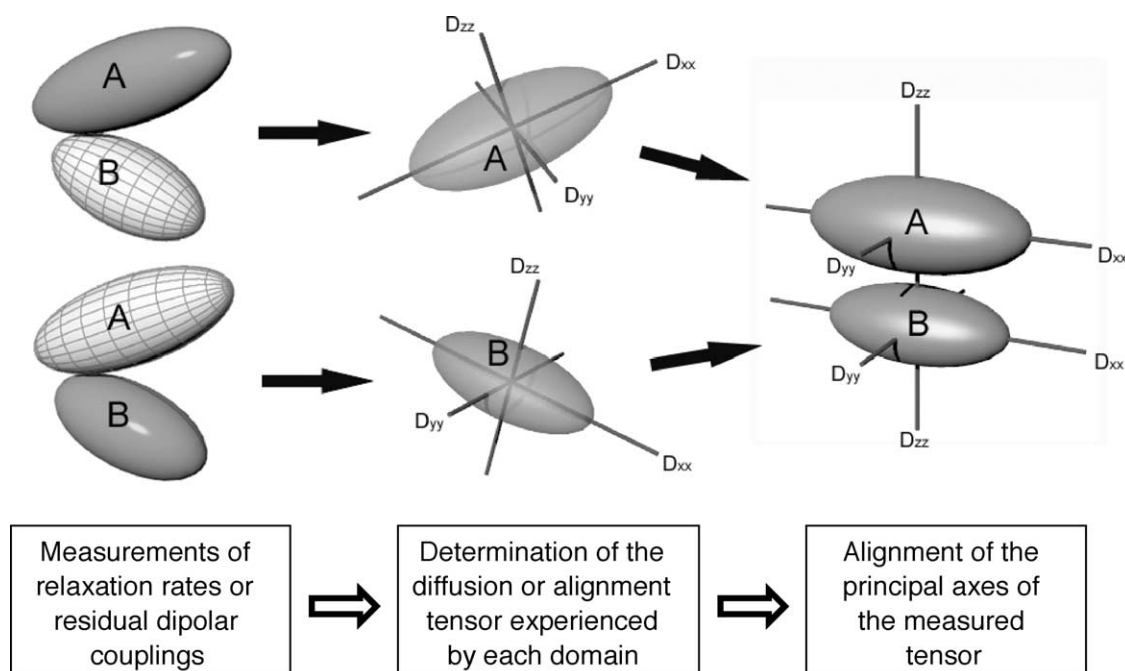orientation of the domains, which depends on the time scale and the extent of interdomain motions in a molecule. Because of the differences in the time windows between the RDC and relaxation measurements, the interdomain orientation obtained by these two methods could be somewhat different.

2.2. Techniques for determining interdomain orientation

Provided the PAFs for each of the domains has been determined (see the following sections), their proper orientation can be achieved using various methods. Here we describe a simple direct approach, based on rigid-body rotation of the domains [2,7]. Another way to achieve the rigid-body alignment of the domains is to include this information as orientational constraints into structure refinement protocols [25], which could also be combined with molecular docking approaches [26,27]. It is also possible to circumvent the determination of the individual tensors by converting the orientation information into intervector restraints, as proposed in Ref. [28].

In general, if the orientation of the tensor PAF with respect to the atom coordinate frame (PDB) of a protein is defined by the Euler angles $\{\alpha, \beta, \gamma\}$, then the rotation matrix [29]

e.g. domain B, such that its coordinates are expressed in the PDB coordinate frame of the other domain (A) :

$$\mathbf{r}_B^A = R^{-1}\{\alpha_A, \beta_A, \gamma_A\}R\{\alpha_B, \beta_B, \gamma_B\}\mathbf{r}_B. \qquad (5)$$

Note that the orientational information available from diffusion or alignment tensors provides interdomain orientation but does not allow proper positioning of the domains with respect to each other in the 3D space, because the interdomain distance is not known. In order to obtain the relative positions of the domains, this information has to be combined with distance or contact-related information, for example, in the form of NOE constraints or chemical shift perturbation maps.

3. Determination of the alignment tensor of a molecule

Dipolar interaction of nuclear magnetic moments depends on the angle between the internuclear vector and the static magnetic field. This coupling cannot be directly observed in NMR spectra in isotropic liquids, because fast molecular tumbling averages the dipolar interaction to zero. If, however, a molecule is partially aligned, i.e. some of its orientations are more likely than

$$R_{\text{PDB}\rightarrow\text{PAF}} = R(\alpha, \beta, \gamma) = \begin{pmatrix} \cos\alpha\cos\beta\cos\gamma - \sin\alpha\sin\gamma & \sin\alpha\cos\beta\cos\gamma + \cos\alpha\sin\gamma & -\sin\beta\cos\gamma \\ -\cos\alpha\cos\beta\sin\gamma - \sin\alpha\cos\gamma & -\sin\alpha\cos\beta\sin\gamma + \cos\alpha\cos\gamma & \sin\beta\sin\gamma \\ \cos\alpha\sin\beta & \sin\alpha\sin\beta & \cos\beta \end{pmatrix}, \qquad (1)$$

will transform coordinates $\mathbf{r} = \{x, y, z\}$ of an arbitrary atom in the protein frame into its coordinates in the PAF frame of the tensor:

$$\mathbf{r}^t = R(\alpha, \beta, \gamma)\mathbf{r}. \qquad (2)$$

This transformation can also be considered as a rotation of the molecule such that the x-, y-, and z-axes of the PAF are now oriented along $\{1\ 0\ 0\}$, $\{0\ 1\ 0\}$ and $\{0\ 0\ 1\}$ directions, respectively.

Applying similar transformations to the individual domains in a protein, e.g. domains A and B :

$$\mathbf{r}_A^t = R\{\alpha_A, \beta_A, \gamma_A\}\mathbf{r}_A, \qquad (3)$$

$$\mathbf{r}_B^t = R\{\alpha_B, \beta_B, \gamma_B\}\mathbf{r}_B, \qquad (4)$$

will rotate both domains (whatever the original orientation of their PDB frames was) so that their coordinates will be transformed into the common PAF frame. As a result, the two domains are now oriented such that the PAFs of the molecule experienced by these domains are aligned. Alternatively, one could rotate only one of the two domains,

the other, this will result in a non-zero average, residual dipolar couplings that could be directly observed [5,6]. This orientational anisotropy could be achieved by using oriented medium (e.g. liquid crystals [6] or gels [30,31]) or as a result of a sufficiently large anisotropy of magnetic susceptibility of the molecule, which would cause it to adopt a preferred orientation with respect to the external magnetic field. The latter is observed in nucleic acids [32] or protein molecules with paramagnetic centers [5, 33–35]. The degree of orientational order introduced by an aligning medium depends on the nature of its interactions with a molecule [36,37]. RDCs depend both on the overall molecular order tensor and on the orientation of the individual vectors relative to the PAF of the tensor (see below), and therefore present an invaluable source of information for structure determination [38]. The applications range from biomolecular structure elucidation [39], conformational analysis of oligosaccharides [40] to analysis of protein–ligand conformation [41,42] and domain orientation in proteins [8,9,13,15].

The residual dipolar coupling between nuclei i and j can be expressed as

$$d_{ij} = d_{ij}^0 \sum_{kl} S_{kl} \cos \alpha_k \cos \alpha_l, \qquad (6)$$

where $\cos \alpha_k$ $(k = x, y, z)$ are the direction cosines for a given internuclear vector $\mathbf{r}_{ij}$ (assumed constant) in the molecular frame,

$$d_{ij}^0 = -\left(\frac{\mu_0}{4\pi}\right) \frac{\gamma_i \gamma_j h}{2\pi^2 r_{ij}^3},$$

is the strength of the (static) dipolar coupling between the nuclei, μ_0 is the magnetic permeability of vacuum, γ_i is the gyromagnetic ratio of spin i, and h is Planck's constant. Here S is the Saupe order matrix [43] which is traceless $(S_{xx} + S_{yy} + S_{zz} = 0)$ and symmetric $(S_{kl} = S_{lk})$. For a molecule with coordinates defined in an arbitrary Cartesian system, the Saupe matrix is given by

$$S_{kl} = \left\langle \frac{3 \cos \zeta_k \cos \zeta_l - \delta_{kl}}{2} \right\rangle,$$

where ζ_k gives the orientation of the kth molecular axis with respect to the director (assumed to coincide with the direction of the static magnetic field) and δ_{kl} is the Kronecker's delta. The angular brackets here denote a time average. The residual dipolar couplings contain valuable structural information (through the angular dependence) as well as dynamic information (through motional averaging) [44]. For a given internuclear vector with the polar coordinates $\{\theta, \phi\}$ in the PAF of the order tensor, Eq. (6) can be rewritten as

$$d_{ij} = \tfrac{3}{4} d_{ij}^0 [A_{zz}(3 \cos^2 \theta - 1) + (A_{xx} - A_{yy}) \sin^2 \theta \cos 2\phi], \qquad (7)$$

where $A_{ii} = (2/3) S_{ii}$ are the principal values of the so-called alignment tensor (ordered here as $|A_{xx}| < |A_{yy}| < |A_{zz}|$).

Provided that at least five independent experimental RDC values are available, Eq. (6) allows, in principle, a complete determination of the alignment tensor, assuming the structure of the molecule is known. Tensor derivation from a set of linear equations is relatively straightforward [45], and we will not discuss its details here. The method used in this study is based on singular value decomposition [45,46]; it is implemented in a computer program ALTENS [13].

4. Determination of the overall rotational diffusion tensor of a molecule

Accurate analysis of the rotational diffusion tensor is essential for accurate domain orientation based on relaxation data. Because the relationship between the characteristics of the diffusion tensor and the measured relaxation rates is not linear, in contrast to the case of residual dipolar couplings (Eq. (6)), the underlying theory and methods for the tensor determination will be discussed here in greater detail.

4.1. Basic equations

Hydrodynamic characteristics and motional properties of a molecule in solution reflect its size and three-dimensional shape. When rotational diffusion of a molecule is anisotropic, i.e. molecule reorients faster around some directions in the molecule than around others, the rates of nuclear spin relaxation (e.g. of ^{15}N, considered here) depend on the orientation of a given group (NH bond) with respect to the principal axes frame of the diffusion tensor [4]. This means that the spin-relaxation rates contain information on both the rotational anisotropy and molecular structure. When the directions of the observed vectors (NH) within a molecule are known, this orientation dependence of the measured relaxation parameters can be used to characterize the overall rotational diffusion of the molecule. Several approaches to the determination of the diffusion tensor from ^{15}N relaxation data have been suggested in the literature [2,3,7,47,48]. The method discussed in detail here uses the orientational dependence of the ratio of the ^{15}N relaxation rates [7,49,50]:

$$\rho = \left(\frac{2R_2'}{R_1'} - 1\right)^{-1} = \frac{3}{4} \frac{J(\omega_N)}{J(0)}. \qquad (8)$$

Here R_1' and R_2' are the rates of longitudinal and transverse relaxation, respectively; the prime indicates that these rates are modified by subtracting the contributions from high-frequency components of the spectral density [51,52]:

$$R_1' = 3(c^2 + d^2)J(\omega_N)$$
$$= R_1[1 - 1.249|\gamma_N/\gamma_H|(1 - \text{NOE})], \qquad (9)$$

$$R_2' = 0.5(c^2 + d^2)[4J(0) + 3J(\omega_N)]$$
$$= R_2 - 1.079|\gamma_N/\gamma_H|R_1(1 - \text{NOE}). \qquad (10)$$

In these equations, terms d and c represent contributions from ^{1}H$-^{15}$N dipolar interaction and ^{15}N chemical shift anisotropy (CSA), respectively, γ_H and γ_N are the gyromagnetic ratios of ^{1}H and ^{15}N, and ω_H and ω_N are the corresponding Larmor frequencies. The spectral densities, $J(\omega)$, contain information about the motions (both overall and local) involving a NH group under observation.

The advantage of using the ratio, R_2'/R_1', instead of the individual values of these parameters is that it is

independent, to a first approximation, of the site-specific variations in the strength of ^{1}H–^{15}N dipolar coupling and ^{15}N CSA. Moreover, for NH groups belonging to well-defined structural regions in a protein the R_2'/R_1' ratio primarily depends on the overall tumbling and is practically insensitive to fast, subnanosecond local dynamics, because the order parameters representing local motions in the numerator and in the denominator of Eq. (8) cancel out [50].

Here we will assume that the modulation of the ^{1}H–^{15}N dipolar and ^{15}N CSA interactions that causes spin relaxation in the NH group results primarily from a 'rigid-body-like' rotation of the dipolar and CSA tensors as a result of the NH-bond reorientation with respect to the static magnetic field. Modulation of the strength of these tensors caused by internal dynamics in the protein will not be considered. Assuming that internal motion is negligible, we then consider only the overall motion, and the relevant correlation function describing anisotropic rotational diffusion is given by Ref. [53]

$$C_{\text{ovrl}}(t) = \frac{1}{5} \sum_{i=1}^{5} a_i \, e^{-tD_i}, \tag{11}$$

where rate constants D_i are related to the principal values of the rotational diffusion tensor $\underline{D}$:

$$
\begin{aligned}
D_1 &= 4D_{xx} + D_{yy} + D_{zz}; \\
D_2 &= D_{xx} + 4D_{yy} + D_{zz}; \\
D_3 &= D_{xx} + D_{yy} + 4D_{zz}; \\
D_4 &= 6D_{\text{iso}} + 6(D_{\text{iso}}^2 - D^2)^{1/2}; \\
D_5 &= 6D_{\text{iso}} - 6(D_{\text{iso}}^2 - D^2)^{1/2}; \\
D^2 &= (D_{xx}D_{yy} + D_{yy}D_{zz} + D_{xx}D_{zz})/3; \\
D_{\text{iso}} &= \text{tr}(\underline{D})/3 = (D_{xx} + D_{yy} + D_{zz})/3.
\end{aligned}
\tag{12}
$$

The coefficients a_i depend on the coordinates $\mathbf{r}^{\text{t}} = \{x^{\text{t}}, y^{\text{t}}, z^{\text{t}}\}$ of a given unit NH vector in the PAF of the diffusion tensor; the analytical expressions for a_i can be found in Ref. [53]. The relationship between $\mathbf{r}^{\text{t}}$ and the vector coordinates $\{x, y, z\}$ in the molecular frame is given by Eq. (2). The corresponding spectral density function is:

$$J(\omega) = \frac{2}{5} \sum_{i=1}^{5} \frac{a_i D_i}{D_i^2 + \omega^2} \tag{13}$$

and the expected values for the relevant spin-relaxation parameters can be obtained by substituting Eq. (13) into Eqs. (9) and (10).

For a symmetric top with an axially symmetric diffusion tensor, $D_\perp = D_{xx} = D_{yy}$ and $D_\parallel = D_{zz}$ are the two unique diffusion coefficients, and the expression for ρ can be simplified [7]:

$$
\rho = \frac{3J(\omega_{\text{N}})}{4J(0)} = \frac{3/4}{1 + (\omega_{\text{N}}\tau_x)^2} \left\{ 1 + \frac{(\omega_{\text{N}}\tau_x)^2}{(\omega_{\text{N}}\tau_x)^2 + (1 + \frac{1}{6}\varepsilon)^2} \right.
$$

$$
\times \frac{\varepsilon \sin^2\theta}{3 + 2\varepsilon + [1 + \frac{1}{3}\varepsilon(2 - 3\sin^2\theta)]^2} \left[4 + 3\varepsilon + \frac{2}{9}\varepsilon^2 \right.
$$

$$
\left. \left. \times -\varepsilon \sin^2\theta \left(1 + \frac{4 + \frac{11}{3}\varepsilon + \frac{19}{18}\varepsilon^2 + \frac{5}{54}\varepsilon^3}{(\omega_{\text{N}}\tau_x)^2 + \left(1 + \frac{2}{3}\varepsilon\right)^2} \right) \right] \right\}. \tag{14}
$$

Here $\varepsilon = (D_\parallel/D_\perp) - 1$, $\tau_x^{-1} = 6D_\perp$, and θ is the angle between an NH bond and the unique axis (associated with $D_\parallel$) of the rotational diffusion tensor:

$$\theta = \cos^{-1}(x\cos\alpha\sin\beta + y\sin\alpha\sin\beta + z\cos\beta). \tag{15}$$

For a spherical top characterized by the isotropic diffusion constant $D_{\text{iso}} = D_{xx} = D_{yy} = D_{zz}$, the spectral density is independent of the orientation of the NH bond vector

$$J(\omega) = \frac{2}{5} \frac{\tau_{\text{c}}}{1 + \omega^2 \tau_{\text{c}}^2},$$

where $\tau_{\text{c}} = (6D_{\text{iso}})^{-1}$.

Here we considered only the overall tumbling and have neglected contributions to $J(\omega)$ from internal dynamics. Computer simulations ([50,54] see also below) show that when local motions are restricted (e.g. in protein core) and independent of the overall motion, the predictions for ρ based on Eqs. (9)–(12) are in excellent agreement with the simulated data that include local dynamics.

It is often convenient to characterize deviations from the isotropy (full symmetry) of the rotational diffusion tensor in terms of its anisotropy ξ and rhombicity η, which for a prolate tensor (i.e. $D_{zz} - D_{yy} \geqq D_{yy} - D_{xx}$) are defined here as:

$$\xi = \frac{2D_{zz}}{D_{xx} + D_{yy}}, \tag{16a}$$

$$\eta = \frac{3}{2} \frac{D_{yy} - D_{xx}}{D_{zz} - \frac{1}{2}(D_{xx} + D_{yy})} = \frac{3}{2} \frac{D_{yy} - D_{xx}}{D_{zz}} \frac{\xi}{\xi - 1}. \tag{17a}$$

The corresponding equations for an oblate tensor $(D_{zz} - D_{yy} < D_{yy} - D_{xx})$ are

$$\xi = \frac{2D_{xx}}{D_{zz} + D_{yy}}, \tag{16b}$$

$$\eta = \frac{3}{2} \frac{D_{yy} - D_{zz}}{D_{xx}} \frac{\xi}{1 - \xi}. \tag{17b}$$

A prolate tensor will be assumed throughout this article, i.e. $\xi \geqq 1$ and $0 \leq \eta \leq 1$.

4.2. Orientation dependence of the ratio of relaxation rates

As mentioned above, the measured ^{15}N relaxation parameters (hence ρ) depend on the orientation of the NH bond vector with respect to the principal axes frame of the diffusion tensor. It is instructional to analyze the angular dependence of ρ, because it contains key information for the derivation of the diffusion tensor. For the axially symmetric tensor ρ depends only on the polar angle θ between the vector and the z axis of the tensor (see Eq. (14)). In the general case of full rotational anisotropy relaxation parameters ρ will also depend on the vector orientation in the $x - y$ plane, given by the azimuthal angle ϕ. The dependence of ρ as a function of θ and ϕ is shown in Fig. 3b for a prolate diffusion tensor. The overall shape of the hilly surface reflects symmetry properties of $\rho(\theta, \phi)$: $\rho(\theta, \phi) = \rho(180° - \theta, \phi)$ and $\rho(\theta, \phi) = \rho(\theta, -\phi) = \rho(\theta, 180° - \phi) = \rho(\theta, \phi - 180°)$, stemming from the fact that the relaxation parameters are not sensitive to the directionality (sign) of the vector coordinates. The actual heights of the 'hills' and depths of the 'valleys' depend on the principal values

$\{D_{xx}, D_{yy}, D_{zz}\}$ of the diffusion tensor. The difference in height between the hilltops and the saddle points in the valleys disappears when $D_{yy} \rightarrow D_{xx}$ and the wavy ridge turns into a single-curved surface for an axially symmetric tensor. The whole surface flattens when $D_{xx}, D_{yy} \rightarrow D_{zz}$ and becomes a horizontal plane in the isotropic case.

In the case of axial symmetry, ρ does not depend on the angle ϕ (Eq. (14)). Therefore, when the axially symmetric model is applied to experimental data for a fully anisotropic tensor, the $\rho(\theta, \phi)$ surface is projected onto an area on the $\rho - \theta$ plane (Fig. 3a). As a result, data points located in various parts of the $\rho(\theta, \varphi)$ surface will appear spread in the vertical direction around the $\rho(\theta)$ fitting curve. The upper and lower boundaries of this area are given by $\phi = 0$ and $90°$ and correspond to those cases when the NH vector is parallel to the $x-z$ or $y-z$ plane, respectively. The gap between the two boundaries varies with the angle θ: negligible for θ close to 0, it increases with the tilt of the vector from the z-axis and reaches maximum when $\theta = 90°$. The top points on the boundary curves correspond to the two limiting cases of the NH vector oriented along the x-axis
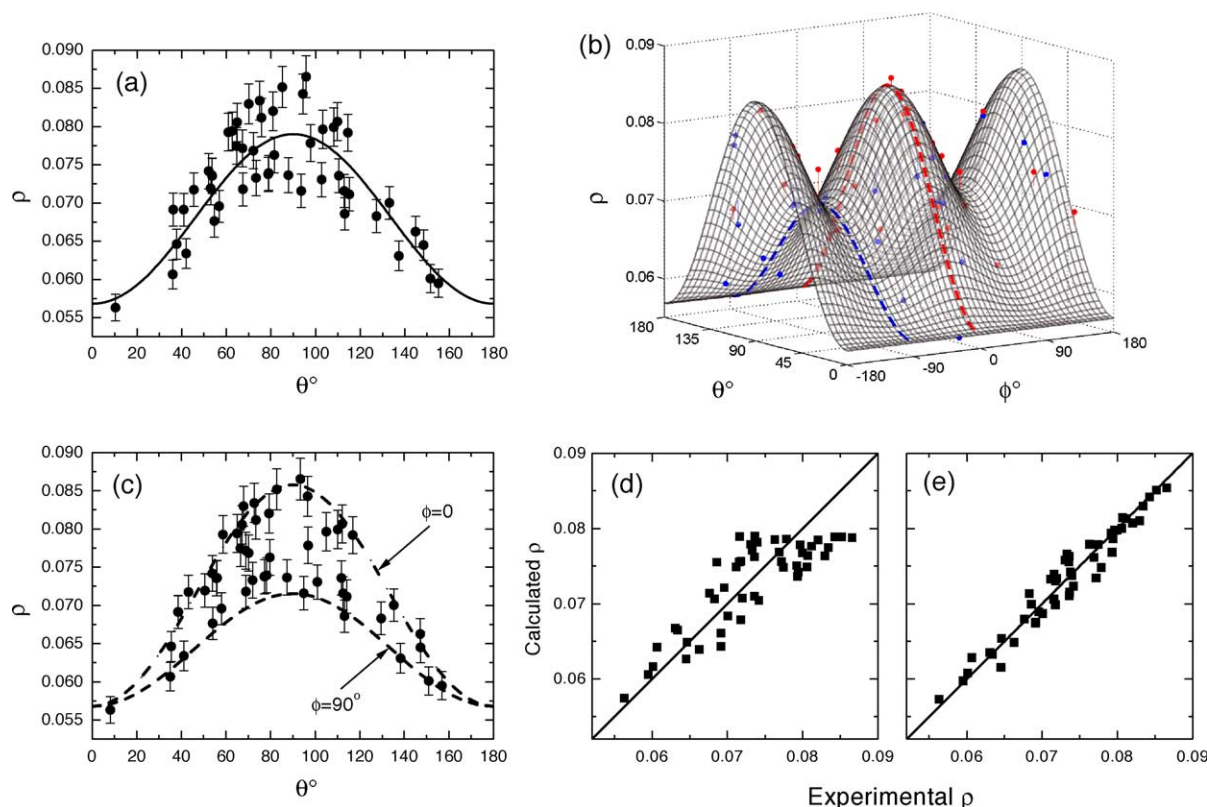
Fig. 3. Orientation dependence of ρ in the case of a fully anisotropic diffusion tensor. Shown here are examples of fitting computer-generated 'experimental' data using (a) axially symmetric (Eq. (14)) and (b,c) fully anisotropic (Eqs. (11)–(13)) rotational diffusion models. The large vertical spread of the data around the fitting curve in panel (a) suggests that this model is not the most adequate one. The fitting surface in (b) reflects the fact that the orientation of a NH vector with respect to the PAF of the diffusion tensor is defined by two angles, θ and ϕ. This hilly surface provides a better fit for the spread in the experimental data. The vertical lines in (b) represent deviations of the data points from their expected positions on the surface. Panel (c) represents a projection of this surface onto the $\theta-\rho$ plane ($\phi = 0$), similar to that in panel (a). This illustrates the fact that the spread of the data points in panel (a) is within the boundaries corresponding to $\rho(\theta)$ for $\phi = 0$ and $90°$ in (b). Relaxation data were generated as described in the text, the tensor parameters are listed in Table 1 for the anisotropy of 1.4 and rhombicity 0.8. Panels (d,e) illustrate the agreement between computer-generated 'experimental' data for a fully anisotropic diffusion tensor and their back-calculated values using (d) axially symmetric and (e) fully anisotropic models of the overall tumbling. A 'flat top' observed in (d) is a characteristic signature of the case when an axially symmetric model is inadequate because it cannot reproduce the dependence of the experimental data on the angle ϕ.

($\rho_x : \theta = 90°$, $\phi = 0$, upper boundary) or along the *y*-axis ($\rho_y : \theta = 90°$, $\varphi = 90°$, lower boundary). The maximal gap then depends on the difference between D_{yy} and D_{xx} (hence the rhombicity η) and can be expressed as

$$\rho_x - \rho_y = \frac{108\eta\omega_N^2 D^2 D_{\mathrm{iso}}(D_{zz} - D_{\mathrm{iso}})}{(D_{\mathrm{iso}} + D_{xx})(D_{\mathrm{iso}} + D_{yy})[(36D^2 + \omega_N^2)^2 + 144\omega_N^2(D_{\mathrm{iso}}^2 - D^2)]}. \tag{18}$$

4.3. Methods for determining the rotational diffusion tensor from ^{15}N relaxation data

Various methods have been applied to retrieve the rotational diffusion tensor from NMR relaxation data. These range from approximate approaches, assuming a small degree of anisotropy [2,47] and linearizing the corresponding system of equations, to accurate approaches, making no simplifying assumptions about the diffusion tensor [7,49,55].

The determination of the diffusion tensor parameters is achieved here by minimizing the target function

$$\chi^2 = \sum_{i=1}^{N_r} \left(\frac{\rho_i^{\mathrm{exp}} - \rho_i^{\mathrm{calc}}}{\sigma_i} \right)^2, \tag{19}$$

where N_r is the total number of NH vectors included in the analysis and σ_i denotes the experimental error in ρ_i for residue *i*. The value of ρ^{exp} can be directly derived from the measured relaxation parameters, according to Eqs. (8)–(10), and ρ^{calc} is calculated using Eqs. (8)–(13) or Eqs. (14) and (15), depending on the rotational model. The minimization of the target function for a fully anisotropic tensor requires an optimization search in a six-dimensional space and could be significantly more computationally intensive than that for an axially symmetric tensor.

In our previous, simplex-based methods [7,49], the optimization was separated into a simplex search in a 3D space of the principal values of the tensor and a grid search in the Euler angle space. This was done to circumvent the problem of implementing periodic boundary conditions for Euler angles in the simplex algorithm. The angular-grid search turned out to be time consuming, particularly in the case of a fully anisotropic tensor. A two-step, hybrid procedure was therefore developed [49], where singular value decomposition (assuming a small degree of anisotropy) is first applied to obtain a preliminary estimate of the diffusion tensor. This estimate is then used as input for the second step that utilizes a combination of simplex and grid searches [7,50,56] in a narrower region of the full 6D space to determine the complete diffusion tensor.

We have recently developed an alternative strategy to determine the full set of diffusion tensor parameters and Euler angles, implemented in our computer program ROTDIF [13]. The novelty of the proposed algorithm over the previous methods [7,50,56] is that the optimization search is performed in a full 6D space. Instead of setting the periodic boundary conditions for the Euler angles we impose strict boundary conditions and restrict the allowed angle space to a 3D box of [0,180] intervals for all three Euler angles. Due to the symmetry properties of the problem (see above), this subspace fully represents all relevant orientations of the tensor frame. Our analysis showed that it is possible to implement this approach in simplex by imposing a severe penalty function for the angle values outside this 3D box. However, the constrained Levenberg–Marquardt method turned out to be robust and more efficient in this case, even when combined with the Monte Carlo screening of the initial guesses (below).

The Levenberg–Marquardt algorithm works very well in practice and has become the standard of non-linear least-squares optimization. It gives accurate results when the initial guess is not far from the global minimum. In order to avoid being trapped in a local minimum, the program generates a set of initial guesses and, for each of them, minimizes the target function χ^2. The program then selects only those values of the fitting parameters that give the lowest value of the target function. Our extensive testing indicates that a set of $\sim$100 random initial guesses is sufficient to find at least one (usually more than a dozen) solution corresponding to the global minimum. The algorithm is so fast that a 6D search including 100 initial guesses for 50 NH vectors takes approximately 20 s elapsed time (i.e. about 0.2 s per guess) on a 1.5 GHz Pentium 4 XEON processor.

The computer program ROTDIF automatically performs data analysis using all three models for the overall rotational diffusion: isotropic, axially symmetric, and fully anisotropic, and determines the most appropriate model based on the statistical *F* test [57]. Because the agreement between experimental data and theoretical model generally improves with the number of adjustable parameters in the model function, the *F*-test helps evaluate whether a decrease in the target function achieved with a larger number of fitting parameters is statistically significant. A large value of *F* justifies the inclusion of the additional terms in the fit. The results can also be represented by the probability *P* that the observed improvement in the $(N + q)$-parameter fit over the *N*-parameter fit is obtained by chance. For the test statistics to be significant at the $(1 - \alpha)\%$ confidence level, *P* should be less than α.

To better assess the agreement between the calculated and the experimental values of ρ, we also included a quality factor similar to that previously defined [49,58]

$$R_\rho = \langle(\rho^{\mathrm{exp}} - \rho^{\mathrm{calc}})^2\rangle^{1/2}/\langle 2(\rho^{\mathrm{exp}} - \langle\rho^{\mathrm{exp}}\rangle)^2\rangle^{1/2}, \tag{20}$$

where the brackets stand for an average over all available NH vectors. $R_\rho \to 0$ when the calculated and experimental values of ρ are close to each other.

4.4. Computer simulations

To analyze in detail the derivation of the diffusion tensor from ^{15}N relaxation data, we first apply this procedure to synthetic relaxation data (R_1, R_2, and NOE) generated for a set of 50 randomly oriented NH vectors The orientations of the vectors were distributed almost uniformly, judging by the low value, 0.0415, of the generalized sampling parameter [59]. The relaxation data were generated assuming an isotropic, axially symmetric, or fully anisotropic model for the overall diffusion tensor. The input characteristics of the tensors are shown in Table 1, along with the results of the analyses. Local dynamics were also included, characterized by the model-free parameters $S^2 = 0.9$ and $\tau_{loc} = 50$ ps, typical for a protein core. A 2% random 'experimental' noise was added to all simulated relaxation parameters. The results (Table 1) show excellent agreement between the derived and the input diffusion tensors, when the proper overall rotational diffusion model is applied.

4.4.1. Characteristic signatures of a fully anisotropic tumbling

Rotational diffusion reflects the shape of a molecule and is anisotropic, in general. Symmetry-based models (isotropic or axially symmetric) significantly simplify data analysis, however, their application requires a validation in each particular case. Therefore, it is important to be able to verify that the applied diffusion model is adequate. Significant attention has already been paid in the literature on how to identify the presence of rotational anisotropy [3,4,60]. The criteria typically used for these purposes include the observation of systematic orientation-dependent variations in ^{15}N relaxation rates in the well-structured regions of a molecule [54] and theoretical predictions for the diffusion tensor [61]. While the presence of rotational anisotropy versus isotropic diffusion is usually readily recognizable, the presence of the rhombic component of the tensor could be more difficult to identify. Therefore, here we use our computer-generated data to discuss characteristic signatures of a fully anisotropic rotational diffusion.

We will consider in detail here the case when an axially symmetric model is applied to fit relaxation data for a fully anisotropic diffusion tensor, with rhombicity of 0.8 (Table 1). In this case we obtained two minima for the target function, which were very close in their χ^2 values and represented prolate and oblate approximations of the tensor. The presence of the two minima has been shown [62] to be a general feature when approximating a truly anisotropic system by an axially symmetric tensor. We could distinguish the prolate from the oblate case by a lower value of the target function (147.7 versus 158.7). The two-minima

problem disappeared when the data were treated using a fully anisotropic model. Moreover, the target function decreased considerably when going from an axially symmetric to a fully anisotropic model, which is generally interpreted as a better fit. The F-test ($F = 94$, Table 1) indicates that there is a 10^{-16} probability that the observed decrease in χ^2 was obtained by chance. Note that the F-test becomes less definitive when the rhombicity is small (e.g. $\eta = 0.2$, Table 1).

The quality of the fit to anisotopic diffusion models is shown in Fig. 3 depicting the angular dependence of the experimental data. The axially symmetric diffusion model yields quite accurate values for the anisotropy of the tensor and for the overall correlation time and predicts the correct orientation for the z-axis of the diffusion tensor (Table 1). However, the fit shows a significant vertical spread of the ρ values around the fitting curve (Fig. 2a), most pronounced around its maximum (at $\theta \sim 90°$), which indicates that the axially symmetric model is not capable of reproducing all features of the 'experimental' data set. Such a spread, when observed in real experimental data (see below), could also be interpreted as a result of experimental noise, so the question we would like to address is: *Is this spread of data due to experimental errors or due to inadequacy of the diffusion model?* A comparison with the results for the fully anisotropic model helps answer this question. The fully anisotropic model is in a much better agreement with the experimental data (Fig. 3b). As discussed above, we have to consider a fitting surface, not just a fitting curve, as the experimental data now depend on both angles θ and ϕ that define the orientation of an NH vector with respect to the diffusion tensor PAF. What appears like a spread in the data points in Fig. 3a, fits nicely the hills and valleys of the $\rho(\theta, \phi)$-surface. This is because applying an axially symmetric model to the fully anisotropic case amounts to fitting data to a surface with no hills or valleys in the ϕ-dimension. Fig. 3c illustrates this issue by showing that the data points in Fig. 3a actually fall within the boundaries (indicated by the dashed curves in Fig. 3b) corresponding to $\phi = 0$ and $\phi = 90°$. This observation suggests that a vertical spread of the data points at $\theta \sim 90°$ in the axially symmetric fit is a characteristic signature of the difference between D_{xx} and D_{yy} (see Eq. (18)) and can be used as an indicator that an axially symmetric model is inadequate.

Fig. 3d shows another characteristic signature of the case when an axially symmetric model is inadequate, and fully anisotropic model is required. Here the correlation plot of the predicted versus the experimental data has a characteristic 'flat top': the upper limit of the calculated ρ values is lower than their maximal experimental values. In the axially symmetric model, max$\{\rho\}$ is set by the top ($\theta = 90°$) of the fitting curve that lies in the middle between the boundaries defined by $\phi = 0$ and $90°$. Therefore, the calculated values of $\rho(\theta)$ at $\theta = 90°$ cannot reach the hilltop as they do for

Table 1
The results of the diffusion tensor determination from computer-generated relaxation data for various input and analysed overall tumbling models

Model	D_{xx}[a]	D_{yy}[a]	D_{zz}[a]	α[b]	β[b]	γ[b]	τ_c[c]	ξ[d]	η[e]	χ^2	F[f]	P[g]	R_ρ[h]
Input model: isotropic	2.08	2.08	2.08	–	–	–	8.0	0	0				
Fully anisotropic	2.05 (0.07)	2.07 (0.07)	2.12 (0.08)	158 (53)	50 (41)	78 (95)	8.00 (0.14)	1.03 (0.04)	0.371 (0.3)	39.9	0.07	0.93	0.68
Axially symmetric	2.06 (0.03)	2.06 (0.03)	2.12 (0.07)	155 (32)	48 (53)	–	8.00 (0.12)	1.03 (0.03)		40.1	1.24	0.3	0.68
Isotropic	2.08 (0.01)	2.08 (0.01)	2.08 (0.01)	–	–	–	8.01 (0.02)			43.3			0.7
Input model: axially symmetric	1.84	1.84	2.57	70	60	–	8.0	1.4	0				
Fully anisotropic	1.83 (0.10)	1.87 (0.09)	2.55 (0.2)	71 (5)	58 (3)	33 (52)	8.0 (0.3)	1.38 (0.12)	0.094 (0.02)	40.1	0.8	0.45	0.29
Axially symmetric	1.85 (0.02)	1.85 (0.02)	2.55 (0.07)	72 (2)	59 (3)	–	8.01 (0.1)	1.38 (0.04)		41.6	125	4×10^{-22}	0.29
Isotropic	2.08 (0.01)	2.08 (0.01)	2.08 (0.01)	–	–	–	8.03 (0.05)			381			0.72
Input model: fully anisotropic	1.79	1.89	2.57	70	60	170	8.0	1.4	0.2				
Fully anisotropic	1.81 (0.07)	1.88 (0.07)	2.57 (0.14)	71 (4)	60 (3)	150 (32)	8.0 (0.2)	1.39 (0.08)	0.15 (0.02)	35.6	2.3	0.12	0.22
Axially symmetric	1.84 (0.03)	1.84 (0.03)	2.57 (0.07)	71 (3)	61 (3)	–	8.0 (0.1)	1.39 (0.04)		39.3	137	6×10^{-23}	0.24
Isotropic	2.08 (0.01)	2.08 (0.01)	2.08 (0.01)	–	–	–	8.02 (0.05)			390			0.72
Input model: fully anisotropic	1.64	2.03	2.57	70	60	170	8.0	1.4	0.8				
Fully anisotropic	1.62 (0.04)	2.03 (0.04)	2.56 (0.05)	72 (4)	59 (2)	166 (6)	8.04 (0.1)	1.40 (0.04)	0.83 (0.04)	28	94	1.3×10^{-16}	0.16
Axial symmetry	1.82 (0.05)	1.82 (0.05)	2.58 (0.14)	72 (5)	61 (7)	–	8.03 (0.25)	1.42 (0.07)		147.7	40	6×10^{-13}	0.40
Isotropic	2.07 (0.02)	2.07 (0.02)	2.07 (0.02)	–	–	–	8.05 (0.06)			538.1			0.72
Input model: fully anisotropic	1.59	2.08	2.57	70	60	170	8.0	1.4	1.0				
Fully anisotropic	1.56 (0.04)	2.07 (0.05)	2.61 (0.06)	70 (4)	59 (3)	170 (6)	8.01 (0.1)	1.44 (0.04)	0.97 (0.06)	52.4	80	2×10^{-15}	0.19
Axially symmetric	1.81 (0.06)	1.81 (0.06)	2.63 (0.17)	69 (7)	62 (9)	–	8.0 (0.33)	1.46 (0.09)		243	29	9×10^{-11}	0.44
Isotropic	2.08 (0.02)	2.08 (0.02)	2.08 (0.02)	–	–	–	8.03 (0.07)			709			0.73

Numbers in the parentheses represent standard errors in the derived parameters. The 'input model' lines list the input tumbling model and the corresponding diffusion tensor parameters.

[a] The principal values of the diffusion tensor, in 10^7 s^{-1}.

[b] The Euler angles $\{\alpha, \beta, \gamma\}$, in degrees, define the orientation of the principal axes frame of the diffusion tensor with respect to the coordinate frame of the generated vector set.

[c] The overall rotational correlation time, $\tau_c = (6D_{iso})^{-1}$, in nanoseconds.

[d] The anisotropy of the diffusion tensor, Eq. (16a).

[e] The rhombicity of the diffusion tensor, Eq. (17a).

[f] The F-value for the F-test comparing the current model with a simpler one (indicated in the row below): fully anisotropic versus axially symmetric or axially symmetric versus isotropic model. Large values of F justify the use of a more complex model.

[g] The probability that an improvement in the fit when applying a more complex model has occurred by chance.

[h] The quality factor, Eq. (20).

the fully anisotropic model. The ρ values predicted using the fully anisotropic model are in good agreement with the 'experimental' data (the correlation coefficient $r = 0.98$, Fig. 3e) whereas the agreement is not as good ($r = 0.84$) for the axially symmetric model (Fig. 3d). The quality factor R_ρ, Eq. (20), is 0.4 when the axial symmetry is assumed and drops significantly ($R_\rho = 0.16$) when a correct, fully anisotropic model is applied.

In the opposite situation, when a more complex, fully anisotropic model was applied to the data simulated assuming an axially symmetric diffusion (Table 1, second example), the Euler angle γ determining the orientation of the x and y axes of the tensor showed a large experimental uncertainty. In addition, according to the F-test, the fully anisotropic model was not statistically better than the axially symmetric one: there was a 45% probability that the marginal decrease in the target function was obtained by chance, and there was no improvement in the quality factor ($R_\rho = 0.29$). Similar conclusions hold when the data for the isotropic model are treated assuming rotational anisotropy (Table 1, first example).

4.4.2. Precision and accuracy of diffusion tensor determination from ^{15}N relaxation data

When using rotational diffusion data for structure determination in multidomain systems and/or to study protein dynamics, it is critical to know the limits of the accuracy and precision in the diffusion tensor determination. The efficient method of full diffusion tensor analysis allowed us to explore the 'ideal-case' limits using computer-simulated data. Here we will focus only on the limitations due to experimental errors. The effect of limited orientational sampling due to a non-uniform distribution of the NH vectors has been discussed elsewhere [59], see also below. Specifically, the question we will address here is: *What are the lowest expected precision and accuracy in the derived diffusion tensor, given the level of experimental errors in relaxation parameters?*

To assess the sensitivity of the derived rotational diffusion tensor to the quality of the experimental data, we generated synthetic sets of ^{15}N relaxation data for the same set of 50 randomly uniformly oriented NH vectors as above, assuming an axially symmetric or fully anisotropic diffusion tensor. The τ_c and the orientation of the tensor were the same as in Table 1. For an axially symmetric model, the anisotropy of the tensor varied from 1.04 to 1.4. For a fully anisotropic model, where both the anisotropy and rhombicity could vary, we performed four sets of simulations. First, the anisotropy was kept constant ($\xi = 1.3$) and the rhombicity η varied from 0.1 to 1.0. Then we varied the anisotropy (from 1.05 to 1.4) for three fixed values of the rhombicity (1.0, 0.4 and 0.2). The levels of experimental error ranged from 1 up to 10%. 500 sets of relaxation data (R_1, R_2, NOE) were generated for each combination of experimental error, anisotropy, and rhombicity. Each generated data set was analyzed assuming axially symmetric or fully anisotropic model. The precision of the derived tensor was computed as the standard deviation over the 500 resulting tensors, while the accuracy was assessed as the deviation of the mean of these tensors from the true (input) value.

Precision. The derived uncertainties in the diffusion tensor parameters are shown in Fig. 4a–d for the axially
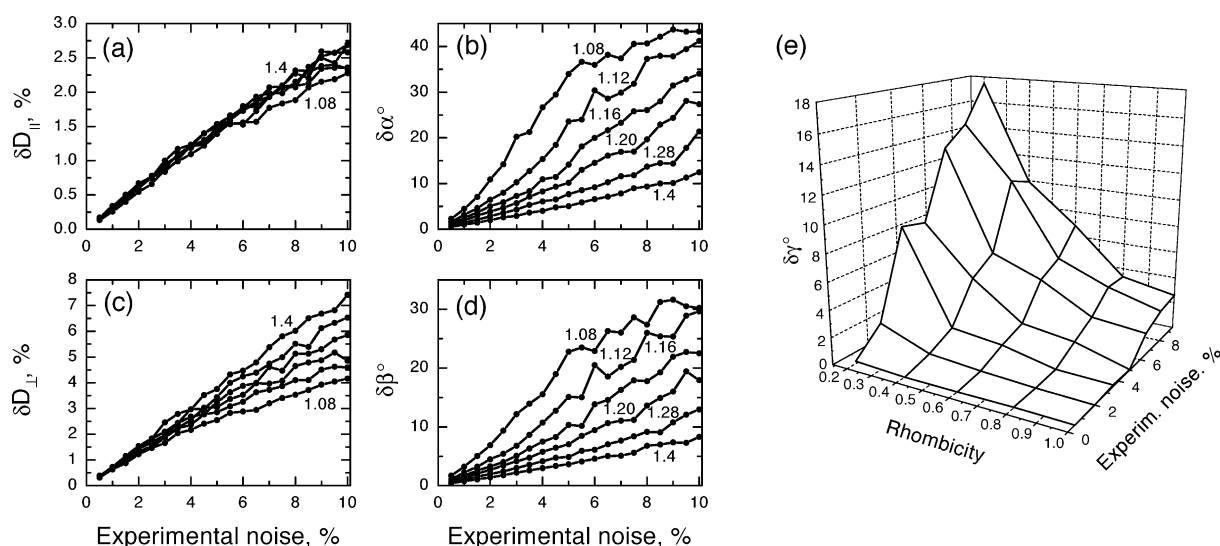

Fig. 4. Illustration of the expected precision (a–d) and accuracy (e) of the derived diffusion tensor parameters as a function of measurement errors in ^{15}N relaxation parameters. The plots represent relative errors (in %) in (a) $D_{\parallel}$ and (c) $D_{\perp}$ and the absolute errors (in degrees) in the angles (b) α and (d) β for various degrees of rotational anisotropy, as indicated. The 'experimental' data for (a–d) were generated and analysed using an axially symmetric model. The input values for the orientation of the tensor ($\alpha = 70°$, $\beta = 60°$) and the τ_c (8 ns) were kept constant. These data indicate that the orientation of the tensor (angles α and β) is more sensitive than its magnitude ($D_{\parallel}$, $D_{\perp}$) to the experimental errors and/or the degree of anisotropy of the tensor. Panel (e) shows the inaccuracy in the determination of the angle γ for various levels of the rhombicity and experimental errors, for a constant anisotropy of 1.3 (fully anisotropic model). The inaccuracy was computed as $|\gamma_{exp} - \langle\gamma_{calc}\rangle|$ where $\langle\cdots\rangle$ denotes averaging over the set of 500 tensor values derived from fitting 500 sets of synthetic relaxation data.

symmetric model. The orientation of the tensor (angles α and β) turned out to be more sensitive than its magnitude (described by $D_\parallel$ and $D_\perp$) to the experimental errors and/or the degree of anisotropy. For a given level of experimental error, the uncertainties in the magnitude of the diffusion tensor increase almost linearly with the decrease in the anisotropy, while the errors in the angles increase faster, as a polynomial function. Similar behavior was observed for the fully anisotropic tensor model. Specifically, for a typical 2% level of experimental precision in R_1, R_2, and NOE, the expected uncertainties in the Euler angles α and β are 4 and 3°, respectively, assuming an axially symmetric model with a relatively small anisotropy of 1.2. The errors in $D_\parallel$ and $D_\perp$ were 0.6 and 1.2%, respectively. These uncertainties decrease for more precise experimental measurements. These data emphasize that the orientation of the diffusion tensor is significantly more sensitive to measurement errors than its principal values. The same tendency was observed in the case of a fully anisotropic tensor (Table 2). Here the angle γ turned out to be most sensitive to experimental errors. Assuming the same anisotropy and experimental errors as above, the uncertainties in γ varied from 17.5 to 5.3° for the range of rhombicities from 0.2 up to the maximum value of 1.0, while the errors in α and β remained practically unaffected (4–6° and 2.5–2.2°, respectively). Under these conditions, the uncertainties in D_{xx}, D_{yy}, and D_{zz} varied from 1.2 to 1.3%, 1.2 to 1.15%, and 1.2 to 1.14%, respectively.

Accuracy. The experimental noise reduces the sensitivity of the analysis, thus making the tensor determination less accurate, even in the case when a correct diffusion model is applied. Our data suggest that, in general, the expected accuracy of the diffusion tensor determination is very good. The observed deviations from the input values were below 0.4% for D_{xx}, D_{yy}, D_{zz} and below 1 and 0.5° for the angles α and β, respectively, for the tensor anisotropy from 1.1 to 1.4 and the rhombicity from 0 to 1, assuming a 2% noise in the experimental data. These inaccuracies increased with the experimental errors and reached 1.4% (D_{xx}), 0.8% (D_{yy}, D_{zz}), and 2.8° (α, β) at a 5% experimental noise level and the lowest considered anisotropy ($\xi = 1.1$). Here again, the angle γ turned out to be the least accurately determined parameter in the fully anisotropic case (Fig. 4e). This angle deviates significantly from its original value when the rhombicity and/or anisotropy are small, hence the orientation of the x and y axes becomes poorly defined. For example, in order to provide a less than 6° inaccuracy in the γ angle, the anisotropy has to be greater than 1.1 (for the rhombicity of 0.4) or greater than 1.2 (for $\eta = 0.2$), assuming a 2% level of the experimental errors.

Sensitivity. The error analysis also allowed us to address the sensitivity issue, i.e. to estimate the lower limits on the tensor's anisotropy and rhombicity that can be reliably determined from the relaxation data. For an axially symmetric model, the lower limit for the anisotropy was $\xi = 1.10$ (for $\tau_c = 8$ ns), defined such that the diffusion

tensor orientation can be determined with better than 10° uncertainty in the angles α and β, given the experimental error of 2%. For the fully anisotropic model, in order to have a less than 10° error in the γ angle, the anisotropy has to be greater than 1.12 (for $\eta = 1.0$) or greater than 1.2 ($\eta = 0.4$), for the same level of experimental errors. Finally, the lowest identifiable rhombicity was 0.3, assuming similar precision criteria (including angle γ) and the anisotropy of 1.3.

5. Structure characterization of di-ubiquitin in solution

5.1. Sample preparation: segmental isotope labeling

Multidomain systems present an additional challenge for NMR data analysis due to crowding in the spectra (hence signal overlap) caused by the presence of NMR signals from several domains. A promising way to solve the crowding problem is to use segmental isotope labeling (reviewed in Ref. [63]), when a specific domain (or a part of it) is isotope labeled, while the rest of the molecule remains unlabeled and hence can be made invisible when applying NMR pulse sequences that allow isotope filtering. The overlap problem is particularly severe in the case of polyUb chains, because all Ub units are expected to be spectroscopically similar. To discriminate between signals from the two Ub domains, Ub_2 chains for this study were assembled from unlabeled and uniformly ^{15}N labeled Ub units, such that in each Ub_2 sample only one specific Ub domain was ^{15}N labeled. Recombinant Ub domains were obtained using bacterial expression in *E. coli* and then assembled in to Ub_2 in a controlled way using E1 and E2 enzymes, as described elsewhere [13,64]. The notations used throughout the text are as follows. Ub_2s are labeled 'P' (i.e. Ub_2-P) for the proximal (with respect to a possible substrate) or 'D' for the distal location of the isotope-enriched Ub moiety in the Ub_2 molecule.

5.2. Relaxation data for Ub_2 and comparison with monoUb

NMR experiments for these studies include measurements of ^{15}N relaxation rates, R_1, R_2, and $\{^1H\} - ^{15}N$ steady-state NOE, using standard pulse sequences [65]. The relaxation delays for Ub_2 studies were typically set to 4 and 920 ms ($\times 4$) for R_1 measurements and 8 and 136 ms ($\times 4$) for R_2, based on the optimal sampling strategy for relaxation measurements [66]. The recycling delay was set to 1.7 s (R_1), 2 s (R_2) and 5 s (NOE). All measurements were performed in sets of interleaved experiments, as described in Ref. [67].

Relaxation experiments were performed at 25 °C. The protein was dissolved in 20 mM sodium phosphate buffer at pH 6.8, also containing 5–20 mM DTT, 1 mM EDTA, 10% ^2H_2O and 0.1% (w/v) NaN_3. The sample concentration varied from 250 μM to 1 mM. At Ub_2 concentrations around or above 1 mM, the measured relaxation rates showed weak

Table 2
The expected imprecision of the diffusion tensor determination as a function of the experimental noise in relaxation measurements and of the tensor's anisotropy and rhombicity

ξ [a]	η [a]	D_{xx} [b]				D_{yy} [b]				D_{zz} [b]				α [c]				β [c]				γ [c]			
		1%	2%	3%	4%	1%	2%	3%	4%	1%	2%	3%	4%	1%	2%	3%	4%	1%	2%	3%	4%	1%	2%	3%	4%
1.12	0	0.37	0.70	1.12	1.38	0.37	0.70	1.12	1.38	0.57	1.12	1.67	2.11	3.1	6.5	10.3	15.4	2.3	4.5	6.8	10.7	–	–	–	–
1.12	0.2	0.62	1.18	2.08	2.76	0.59	1.19	1.97	2.64	0.57	1.13	1.71	2.17	3.4	6.8	11.4	14.7	2.1	4.2	6.4	9.0	15.3	24.6	24.5	28.6
1.12	0.4	0.61	1.14	1.94	2.67	0.58	1.13	1.85	2.57	0.57	1.13	1.69	2.19	3.6	7.3	11.3	16.1	2.0	4.0	6.0	8.5	7.8	13.6	20.0	23.0
1.12	1	0.65	1.20	1.71	2.42	0.58	1.20	1.75	2.37	0.59	1.14	1.63	2.33	4.5	9.9	15.1	19.1	1.7	3.6	5.6	7.4	3.8	7.9	10.9	14.3
1.2	0	0.37	0.77	1.08	1.42	0.37	0.77	1.08	1.42	0.55	1.19	1.64	2.23	1.9	3.9	5.7	8.3	1.4	2.7	4.2	5.7	–	–	–	–
1.2	0.2	0.60	1.21	1.87	2.53	0.60	1.21	1.81	2.48	0.55	1.19	1.64	2.28	2.0	4.1	6.1	8.7	1.3	2.5	3.9	5.5	8.9	17.5	22.1	24.4
1.2	0.4	0.61	1.20	1.80	2.42	0.60	1.21	1.70	2.38	0.55	1.19	1.64	2.28	2.2	4.4	6.5	9.3	1.2	2.4	3.7	5.2	5.1	9.7	15.4	17.3
1.2	1	0.65	1.30	1.92	2.48	0.56	1.15	1.76	2.21	0.55	1.14	1.68	2.21	3.0	6.1	8.4	12.0	1.1	2.2	3.2	4.5	2.6	5.3	7.3	9.0
1.32	0	0.39	0.74	1.11	1.42	0.39	0.74	1.11	1.42	0.59	1.07	1.59	2.13	1.3	2.5	3.9	5.1	0.8	1.7	2.6	3.5	–	–	–	–
1.32	0.2	0.62	1.23	1.93	2.49	0.58	1.20	1.80	2.45	0.59	1.09	1.59	2.16	1.4	2.6	4.1	5.4	0.8	1.6	2.5	3.4	6.2	12.1	16.8	21.9
1.32	0.4	0.64	1.27	1.92	2.40	0.58	1.20	1.73	2.37	0.59	1.09	1.59	2.16	1.5	2.9	4.5	5.8	0.8	1.6	2.4	3.2	3.4	6.6	9.0	11.9
1.32	1	0.67	1.39	2.04	2.64	0.58	1.12	1.71	2.27	0.55	1.10	1.63	2.31	2.0	3.8	5.7	8.0	0.7	1.4	2.1	2.9	1.7	3.3	4.7	6.5
1.4	0	0.36	0.76	1.22	1.54	0.36	0.76	1.22	1.54	0.52	1.10	1.76	2.12	1.0	2.0	2.9	4.0	0.7	1.4	2.2	3.0	–	–	–	–
1.4	0.2	0.64	1.26	2.02	2.61	0.59	1.20	1.88	2.49	0.52	1.11	1.78	2.15	1.1	2.1	3.1	4.3	0.7	1.4	2.1	2.8	5.1	9.7	16.0	19.0
1.4	0.4	0.65	1.30	2.01	2.56	0.59	1.20	1.85	2.41	0.52	1.11	1.78	2.15	1.2	2.3	3.4	4.6	0.7	1.3	2.0	2.6	2.6	5.4	7.6	10.3
1.4	1	0.69	1.37	2.07	2.85	0.58	1.17	1.77	2.21	0.55	1.13	1.64	2.13	1.6	3.1	4.4	6.2	0.6	1.1	1.8	2.4	1.3	2.6	3.9	5.3

The errors in the diffusion tensor parameters were computed as a standard deviation over 500 diffusion tensors determined from analysis of 500 computer-generated sets of 'experimental' data (for each of the 50 NH vectors) simulated for each combination of anisotropy, rhombicity, and the level of experimental noise.
[a] Input values of the anisotropy (ξ) and rhombicity (η). The overall rotational correlation time τ_c and the orientation of the tensor were the same as in Table 1.
[b] Relative errors, in percent, in the derived principal values of the diffusion tensor; the four columns correspond to various levels of experimental noise in the relaxation data, as indicated.
[c] Absolute errors, in degrees, in the derived orientation (Euler angles) of the diffusion tensor; the four columns correspond to various levels of experimental noise in the relaxation data, as indicated.

concentration dependence, likely due to intermolecular Ub–Ub interactions. To avoid possible artifacts due to these interactions, the concentrations were lowered, and the effect was monitored by measuring proton T_2 values and ^{15}N relaxation rates, until no change with concentration was observed. The final concentration of Ub$_2$ chains used for these studies was 250 μM.

The measured ^{15}N relaxation data for Ub$_2$ (at pH 6.8) are shown in Fig. 5, together with those for monoUb, for comparison. Higher R_2 and lower R_1 values compared to monoUb reflect slower overall tumbling rate due to higher molecular weight of Ub$_2$. The site-specific variations in the ρ-values are more pronounced in Ub$_2$, suggesting a higher degree of rotational anisotropy than for monoUb. This pattern differs between the two domains in Ub$_2$ and between Ub$_2$ and monoUb, suggesting different orientations of the PAF of the diffusion tensor in all these cases.

5.3. Characteristics of the rotational diffusion tensor for Ub$_2$

The overall rotational diffusion tensors were derived from ^{15}N relaxation data for each Ub unit in Ub$_2$ using the ROTDIF procedure described above. A representative example of data fitting is shown in Fig. 6 for the proximal domain at pH 6.8. The characteristics of the derived diffusion tensors for Ub$_2$ at pH 4.5 and 6.8 are presented in Table 3, and the axes of the diffusion tensor of Ub$_2$ determined for each individual Ub domain are shown in Fig. 7.

5.4. Can Ub$_2$ be considered a single tumbling entity in solution?

Several features of our ^1H and ^{15}N relaxation measurements indicate that both the open and closed conformations of Ub$_2$ correspond to relatively compact states, with the two Ub units tumbling as one entity (i.e. as a dumbbell) rather than as independent 'beads on a string'. First, the ^1H T_2 values measured in Ub$_1$ (50 ms), Ub$_2$ (22–23 ms at pH 6.8 and 25–26 ms at pH 4.5), and Ub$_4$ (13 ms at pH 6.8) are inversely proportional to the molecular weight of the chain. Second, similar behavior is observed in the average level of ^{15}N T_2 values and for the values of $1/\rho$ for each Ub domain that are approximately two-fold shorter in Ub$_2$ compared to Ub$_1$ (Fig. 5). Also the experimental ^{15}N T_1 values are
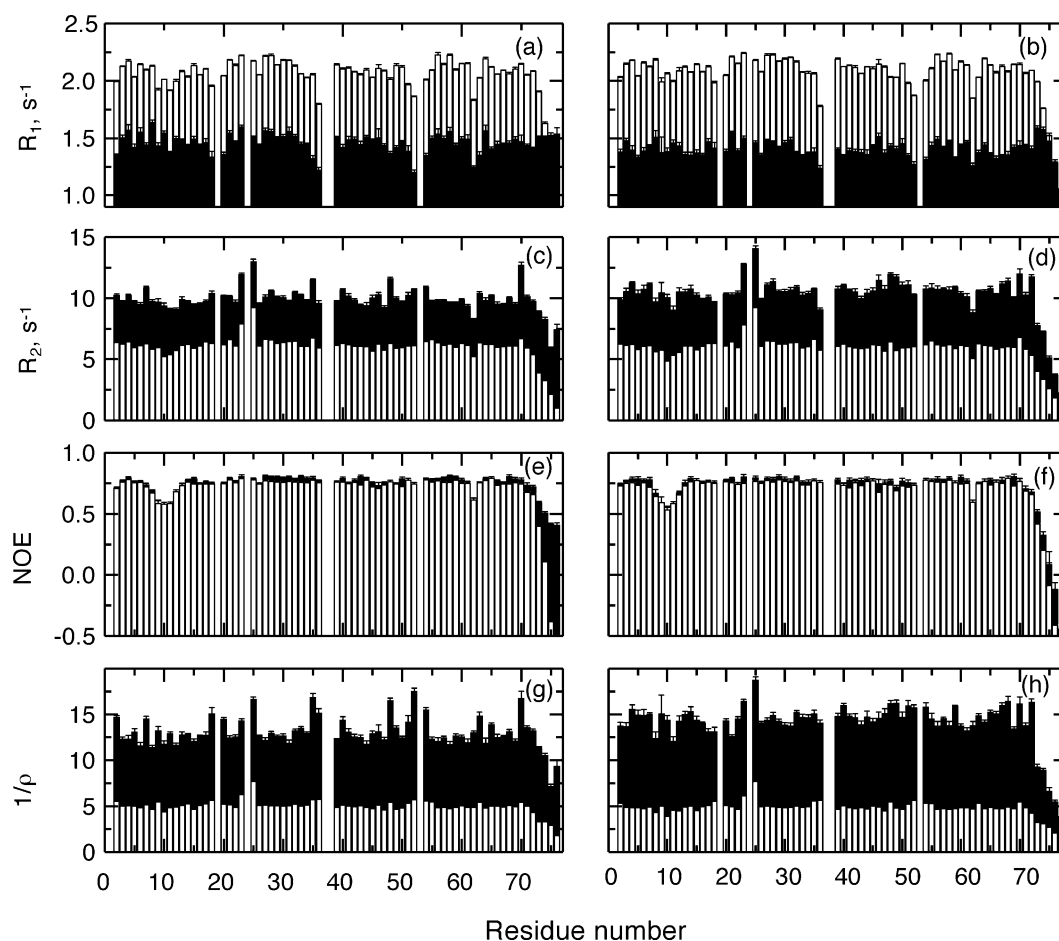

Fig. 5. Experimental ^{15}N relaxation data for the individual domains in Ub$_2$ (pH 6.8): (a,b) R_1, (c,d) R_2, (e,f) heteronuclear NOE, and (g,h) $1/\rho$ (all solid bars). The average experimental precision was 2% (R_1, R_2 and NOE). Shown as open bars are analogous experimental data for the corresponding monoUb constructs, for comparison. Left panels correspond to the distal domain, right panels represent the proximal Ub.
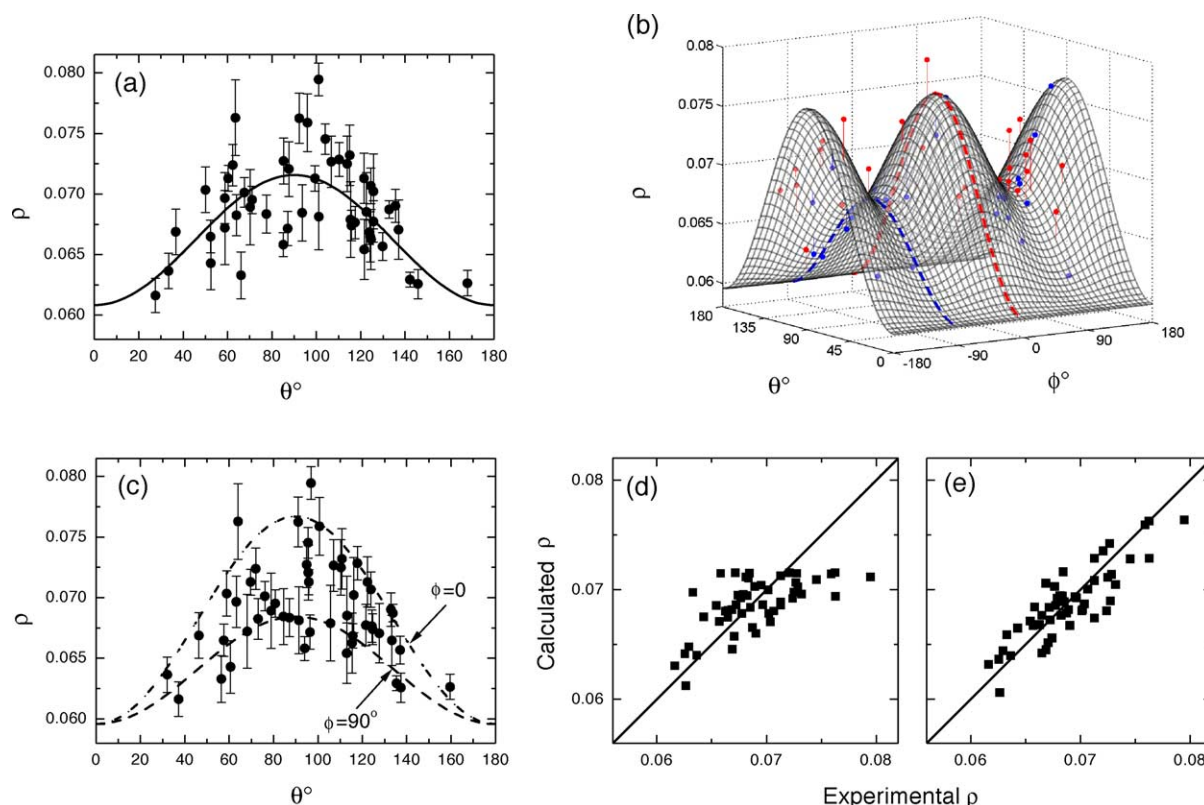
Fig. 6. Details of the diffusion tensor analysis for the proximal Ub domain in Ub_2 (pH 6.8). Shown are the orientation dependence of ρ obtained using (a) axially symmetric and (b,c) fully anisotropic models for the diffusion tensor, and the agreement between the experimental and calculated values of ρ for (d) axially symmetric and (e) fully anisotropic models. Panel (c) is a projection of the surface in (b) onto the $\rho - \theta$ plane; the dashed lines in (b) and (c) represent the upper and lower boundaries corresponding to $\rho(\theta)$ for $\phi = 0$ and 90° (also see Fig. 3).

considerably longer in Ub_2 compared to Ub_1. Finally, the overall rotational correlation times derived from our ^{15}N relaxation data (Table 3) for both Ub domains are two times greater than that (4.2 ns) for the monomeric Ub. All these data suggest that the two domains in Ub_2 are tumbling as one molecule, which then validates the domain orientation approach applied here.

5.5. Alignment tensor determination from RDC measurements in Ub_2

The conformation of Ub_2 at pH 6.8 was also determined using residual dipolar couplings measured in a dilute liquid crystalline phase [68]. The aligning medium was composed of a mixture of n-alkyl-poly(ethylene glycol) ($C_{12}E_5$) and

Table 3
Characteristics of the overall rotational diffusion tensor of Ub_2 at neutral and acidic pH, determined from ^{15}N relaxation data for the two Ub units

Ub unit	D_{xx}[a]	D_{yy}[a]	D_{zz}[a]	α[b]	β[b]	γ[b]	τ_c[c]	ξ[d]	η[d]	P[e]
pH 6.8										
Ub_2-P	1.75 (0.06)	2.00 (0.06)	2.31 (0.06)	105 (8)	112 (9)	135 (11)	8.26 (0.14)	1.23 (0.04)	0.87 (0.11)	3×10^{-12}
Ub_2-D	1.79 (0.10)	1.92 (0.06)	2.63 (0.12)	113 (9)	143 (4)	150 (18)	7.89 (0.21)	1.42 (0.08)	0.24 (0.03)	7×10^{-14}
pH 4.5										
Ub_2-P	1.78 (0.05)	1.99 (0.06)	2.16 (0.06)	39 (13)	38 (13)	124 (18)	8.44 (0.14)	1.15 (0.04)	1.15 (0.20)	2×10^{-12}
Ub_2-D	1.70 (0.08)	1.78 (0.07)	2.49 (0.13)	102 (10)	157 (4)	155 (24)	8.37 (0.24)	1.43 (0.09)	0.172 (0.02)	2×10^{-18}

[a] The principal values of the diffusion tensor (D_{xx}, D_{yy}, D_{zz}) are in $10^7 \, s^{-1}$.

[b] The Euler angles $\{\alpha, \beta, \gamma\}$ characterize the orientation of the principal axes frame of the diffusion tensor of Ub_2 experienced by each of Ub domains. These angles (in degrees) are determined with respect to the PDB coordinate frame (1D3Z.pdb [83]) for each domain.

[c] The overall rotational correlation time of the molecule, $\tau_c = 1/(2 \, tr(\underline{D}))$, in nanoseconds.

[d] Anisotropy (ξ) and rhombicity (η) of the derived diffusion tensor, see Eqs. (16) and (17).

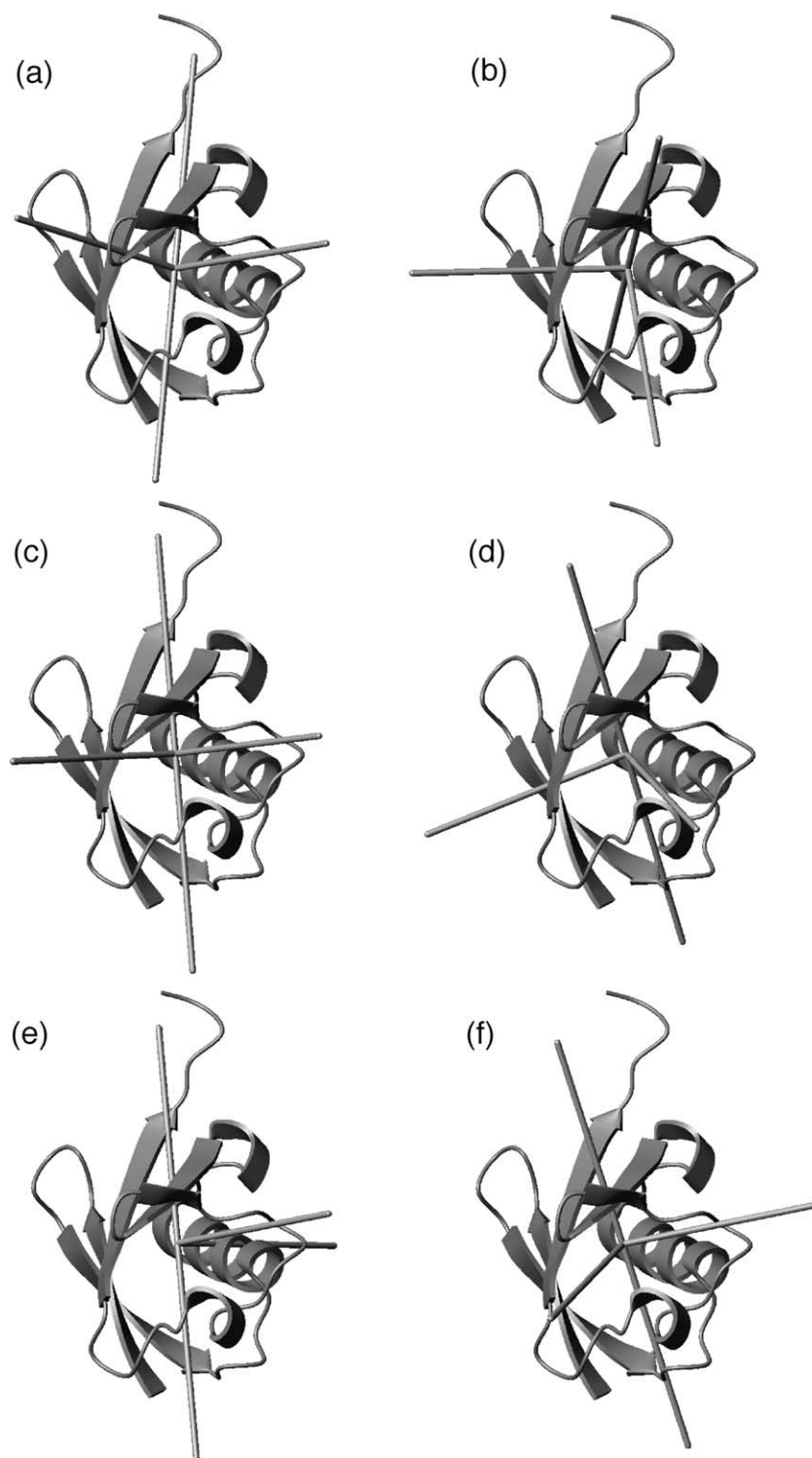[e] The probability that an improvement in the fit compared to the isotropic model occurred by chance.

Fig. 7. Orientation of the (a–d) diffusion and (e,f) alignment tensor axes (shown as rods) of Ub$_2$ determined for each of the domains, as described in the text. Panels (a,b) correspond to Ub$_2$ conformation at pH 4.5, the rest corresponds to pH 6.8. Left panels depict the distal domain, right panels represent the proximal domain. The *z*-axis is shown as the longest rod, extending in both negative and positive directions, while *x*- and *y*- are shown as half-axes. These drawings were generated using MolMol [82].

n-hexanol (molar ratio 0.85) added to the buffer solution at 5 wt% as described in Ref. [69]. The RDCs were obtained from the difference in the ^{15}N–^{1}H couplings observed in the oriented (25 °C) and in the isotropic phase (35 °C).

The ^{1}H–^{15}N couplings were measured using the IPAP ^{1}H–^{15}N HSQC experiment [70] and extracted using the approximation of contour levels by ellipses [71]. The ^{2}H residual quadrupolar splitting of the ^{2}H$_2$O signal in
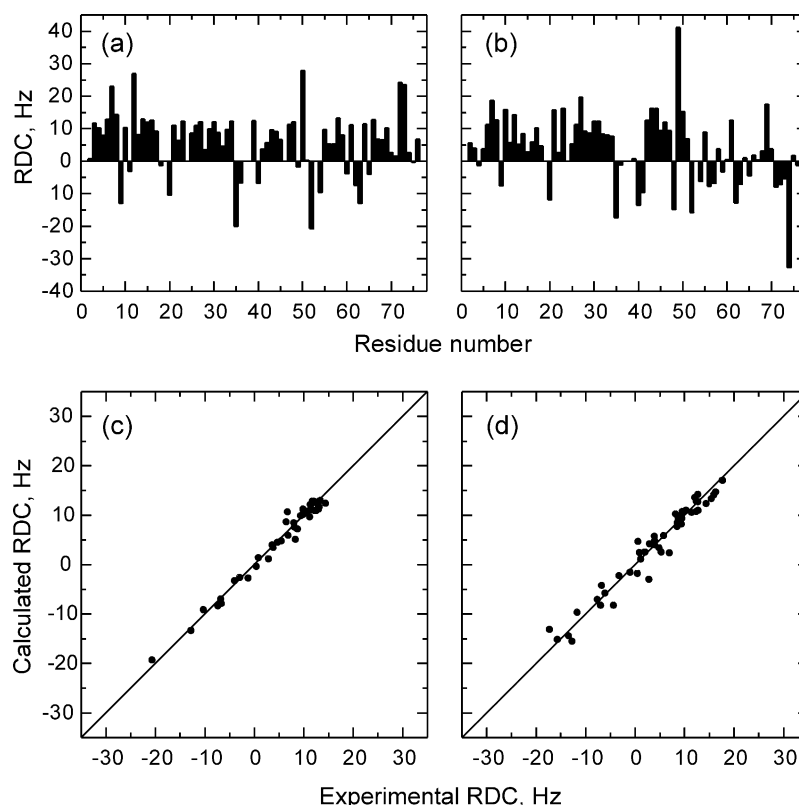
Fig. 8. Details of the alignment tensor analysis for Ub domains in Ub$_2$ (pH 6.8). Panels (a) and (b) depict the experimental RDC values versus residue number. Panels (c) and (d) represent the agreement between the measured and calculated data for protein core residues, the correlation coefficient is 0.99 (c) and 0.98 (d), the quality factors are shown in Table 4. Left panels (a,c) correspond to the distal domain, right panels (b,d) represent the proximal Ub. The atom coordinates for each Ub domain were taken from NMR solution structure 1D3Z.pdb [83].

the ordered phase was ∼21 Hz. The observed RDC values are shown in Fig. 8.

The order tensor $\underline{S}$ was derived from measured RDC values (Eq. (6)) using an in-house program ALTENS based on the singular value decomposition method [45]; the errors were assessed using 10,000 Monte Carlo simulated data sets. The alignment tensor parameters are shown in Table 4.

The excellent agreement between the experimental and back-calculated RDC values (Fig. 8) indicates that the Ub

fold is fully preserved in Ub$_2$. This then validates the use of atom coordinates obtained for monoUb as a structure representation for the individual domains in Ub$_2$. A similar agreement was obtained [13] when using structures of the individual Ub units observed in Ub$_2$ crystals [22].

Note an excellent agreement between the orientation of the z-axes for the diffusion and alignment tensors for each Ub domain in Ub$_2$ at pH 6.8. In general, the PAFs of the diffusion and alignment tensors do not have to coincide, because the solute's alignment depends on the nature of its

Table 4
Characteristics of the alignment tensor for Ub$_2$ at pH 6.8, determined from the residual dipolar couplings for the two Ub units using protein atom coordinates from 1D3Z.pdb [83]

Ub unit	A_{xx} [a]	A_{yy} [a]	A_{zz} [a]	α [b]	β [b]	γ [b]	γ^* [c]	R [d]
Ub$_2$-P	2.1 (0.2)	5.5 (0.2)	−7.4 (0.2)	114 (1)	120 (1)	190 (3)	130 (3)	0.14
Ub$_2$-D	3.2 (0.2)	4.1 (0.2)	−7.3 (0.2)	115 (2)	144 (1)	259 (10)	139 (10)	0.09

[a] The principal values (in 10^{-4}) of the alignment tensor, Eq. (7), calculated assuming $d_{NH}^0 = 21.7$ kHz.

[b] The Euler angles $\{\alpha, \beta, \gamma\}$, in degrees, characterize the orientation of the principal axes frame of the alignment tensor of Ub$_2$ with respect to the PDB coordinate frame for each domain.

[c] The angles γ^* were obtained as $\gamma - 60°$ (Ub$_2$-P) and $\gamma + 60°$ (Ub$_2$-D), which corresponds to a 60° rotation of the x-, y-axes of the alignment tensor for the whole Ub$_2$ molecule about its z-axis (also, γ^* was replaced with $180° + \gamma^*$ for Ub$_2$-D, based on the symmetry properties of the tensor orientation). This transformation has no effect on the relative orientation of Ub units and merely represents the difference in the orientation of the x, y axes of the diffusion and alignment tensors for Ub$_2$. These modified γ-angles agree, within the experimental precision, with those for the rotational diffusion tensor (Table 3).

[d] Quality factor R [58] was used to assess the quality of the derived alignment tensor. The validity of the structural data obtained here is justified by the low values of R indicating good agreement between the measured RDC values and those predicted from the structure.

interaction with the aligning medium. The agreement between the orientations of the two tensors observed here is consistent with the prediction [36,37] that in a neutral aligning medium, such as the one used here, protein alignment is caused by steric interactions, and therefore, is defined by the protein's shape. Even in this case one could expect different orientation of the x, y axes of the two tensors, depending on how the corresponding principal values are defined. All principal values of the diffusion tensor are positive, and are usually defined such that $D_{zz} \geqq D_{yy} \geqq D_{xx}$. The principal values of the alignment tensor can be defined in a similar way, assuming that A_{xx} and A_{zz} represent the two extremes and A_{yy} lies in between. This gives $A_{zz} > A_{yy} \geqq A_{xx}$ or $A_{xx} \geqq A_{yy} > A_{zz}$, depending on the sign of A_{zz}, usually defined as the largest (by the absolute value) principal component of the tensor. Because the alignment tensor is traceless, A_{zz} must be of the opposite sign compared to the other two components, A_{xx} and A_{yy}. Therefore, if sorted by the absolute value (as it is done here and typically assumed in the literature, e.g. [38]), the same tensor components will be ordered as $|A_{zz}| > |A_{xx}| \geqq |A_{yy}|$. This means that if the alignment tensor components are defined according to their absolute values, see Eq. (7), the A_{xx} and A_{yy} components and the corresponding x- and y-axes of the alignment tensor will be swapped. In this case, the orientation of the x-, y-axes of the alignment tensor is expected to differ from that of the diffusion tensor by a 90° rotation about the tensor's z-axis. As can be seen from Fig. 7 and Table 4, the orientations of the x- and y-axes of the two tensors are different. These differences are correlated for both domains, so that the x-, y-axes of the diffusion and alignment tensors could be superimposed (within experimental errors) by a simple simultaneous rotation by $\sim 60°$ of the PAFs for both domains around the z-axis. This rotation does not affect the interdomain orientation and merely indicates different orientation (angle γ) of the rhombic components of the diffusion and alignment tensors. The deviation of this angle from 90° probably reflects the role that the shape of the molecule and other factors (including possible specific interactions with the aligning medium) play in the molecular alignment.

5.6. Domain orientation in Ub₂ from diffusion and alignment tensor measurements

We then used the PAFs of the diffusion or alignment tensors measured in the distal and proximal Ub domains in order to determine their relative orientation in Ub₂. The resulting interdomain orientations are shown in Fig. 9. These structural data show strikingly different solution conformations of Ub₂ depending on pH: an open conformation at acidic conditions and a closed conformation at neutral pH. In the latter conformation, according to our domain orientation data, the hydrophobic patches on the two domains are facing each other and can form an interdomain interface. The chemical shift perturbation
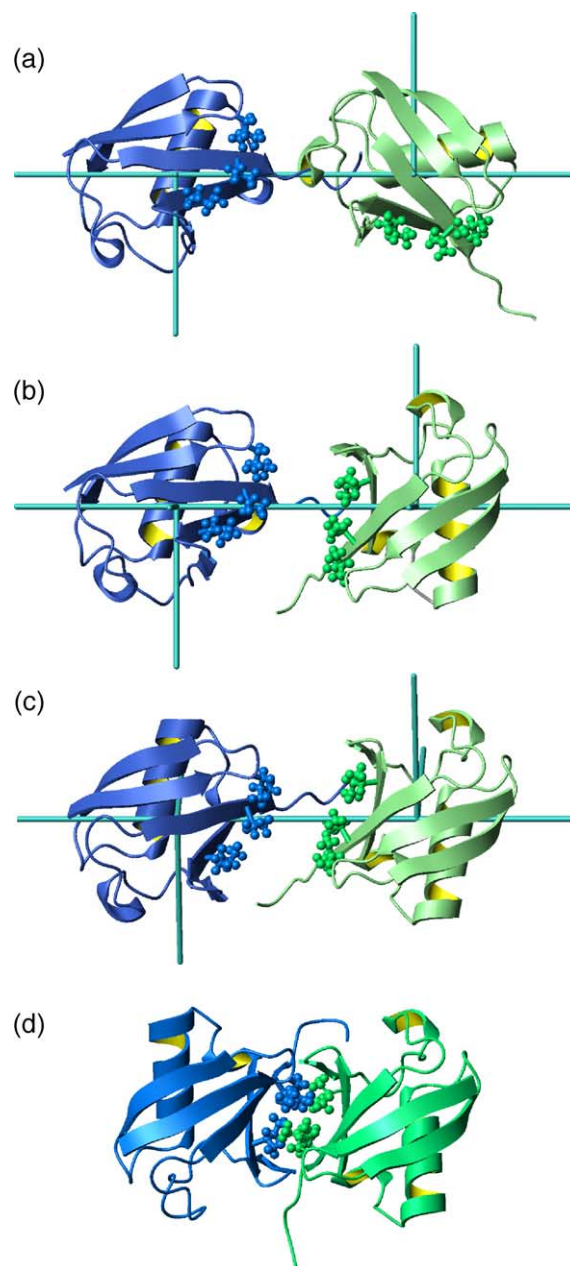

Fig. 9. Solution conformations of Ub₂ derived from (a,b) diffusion (pH 4.5 and pH 6.8), and (c) alignment tensor measurements. Panel (d) represents the crystal structure of Ub₂ obtained at pH 4.5, for comparison. Shown in ball-and-stick representation are side chains of the functionally important residues L8, I44, and V70 that form a hydrophobic patch on the surface of ubiquitin. Rods represent the principal axes of the diffusion or alignment tensors for each of the domains (cf. Fig. 7), the z-axes are in plane and oriented horizontally. The distal domain is colored blue; the proximal domain is green. The Ub₂ conformation at pH 6.8 is characterized by a well-defined interface formed by the hydrophobic patches on the individual Ub units, while at pH 4.5 the chain adopts an open conformation with no contact between the hydrophobic surfaces of the two domains. Because this approach provides the orientation (not the distance) between the domains, their relative positions along the z-axis in (a)–(c) are somewhat arbitrary. Also, the C-termini are unstructured/flexible and should easily adopt a conformation accommodating closer contact between the units. Their conformation shown here is from the monoUb structure and should be considered as an illustration only. These drawings were generated using MolMol [82].
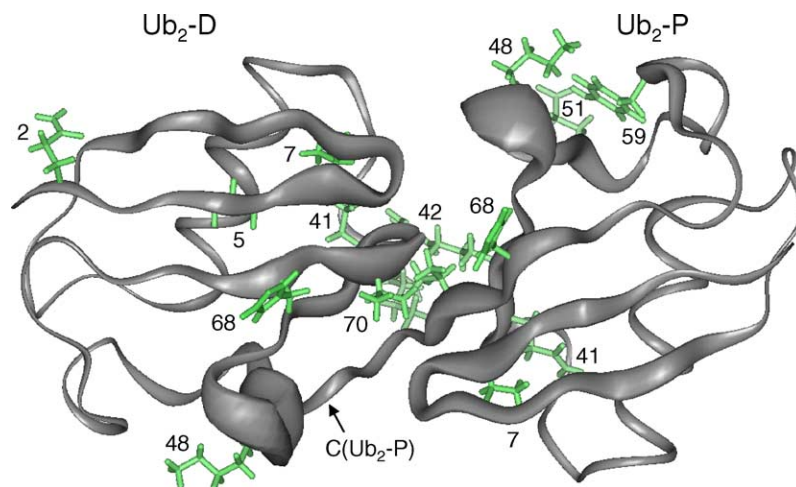
Fig. 10. The solution conformation of Ub$_2$ at pH 6.8 is consistent with the chemical shift perturbation mapping of the interdomain interface. Shown is a cartoon representation of the Ub$_2$ conformation derived from RDC measurements (Fig. 9c), with the ribbon width proportional to chemical shift perturbations observed in Ub$_2$ versus monoUb. Also shown (in stick representation) are side chains for those residues (indicated) involved in conformational exchange in Ub$_2$ (Table 5). The C-terminal residues R72–G76 in the distal domain are not shown: the strong chemical shift perturbations observed here reflect chemical modification of the C-terminus associated with the formation of the isopeptide bond between G76 (Ub$_2$-D) and the side chain of K48 of the proximal domain.

data (Figs. 1 and 10) indeed confirm that the interface is formed, so that in the closed conformation of Ub$_2$ the functionally important hydrophobic residues L8–I44–V70 are buried, while in the open conformation these are readily accessible for possible interactions with ligands. The observation [13] that the relative populations of the closed and open states of Ub$_2$ can be controlled by pH suggests that this pH dependent switch in Ub$_2$ conformation could have functional significance as a mechanism of regulation of ligand binding to polyUb chains.

Interestingly, an open conformation was also observed for the Ub$_2$ chain linked via K63 [15]—these alternatively linked chains are implicated in a variety of non-proteolytic processes, including post-replicative DNA repair in the *RAD6* pathway [72,73], IκBα kinase activation [74], translational regulation [75], and some instances of endocytosis [76].

The Ub$_2$ conformations (pH 6.8) derived from the diffusion and alignment tensors are very similar (Fig. 9b and c, Tables 3 and 4); the small differences in the domain orientation are practically within the experimental errors. For example, if the distal domains from the two structures are aligned, the proximal domains can be almost super-imposed by a set of subsequent rotations of the proximal domain of the diffusion-derived structure (Fig. 9b) by 18° around the z-axis of this molecule and by 10 and 4° around the other two orthogonal axes. This agreement between the results of the two independent methods strongly supports our structural data.

Some difference between Ub$_2$ conformations derived from diffusion and alignment tensors is not unexpected and could reflect different averaging of the structural information by RDC and relaxation measurements in the presence of exchange between the (major) closed and

(minor) open conformations. Note also that both the alignment and diffusion tensors for the distal domain appear more axially symmetric, hence there is greater uncertainty in the γ angle for this domain. This could reflect additional conformational freedom related to the domain's rotation, associated with the Euler angle γ, about the z-axis, which has approximately the same (within 10°) orientation for both the diffusion and alignment tensors. The apparent axial symmetry of the distal domain is likely to be related to the equilibrium between the Ub$_2$ conformations, as the effect is more pronounced at acidic pH where the open conformation is more populated. The observed difference between the rotational/alignment characteristics of the two domains could also reflect intrinsic conformational and/or dynamic properties of Ub$_2$ that depend on how the two Ub units are linked.

5.7. Comparison of the NMR derived structures with the crystal structure of Ub$_2$

The closed-state conformations of Ub$_2$ in solution are similar to the crystal structure [22], in that the hydrophobic patches comprising residues, L8, I44, and V70, from both Ub domains form the interdomain interface (Fig. 9b–d). A close analysis indicates that the interdomain orientation in solution is distinct from that in the crystals. The z-axes of the diffusion tensor derived separately for the two Ub domains using Ub$_2$ crystal structure (1AAR.pdb, [22]) are tilted from each other by 33°. Moreover, when ^{15}N relaxation data for the two domains were fitted together, the target function value per degree of freedom (χ^2/df $= 4.6$) was higher than the corresponding numbers for the distal (3.0) and the proximal (2.0) domains; the probability that this increase in χ^2/df occurred by chance was 0.06 and

0.002, respectively. Finally, the angle between the α-helices in the two Ub domains in solution is 161° (diffusion, Fig. 9b) or 145° (alignment, Fig. 9c), compared to a 128° angle in the crystal structure (Fig. 9d).

Given the fact that the crystals were grown at the conditions (pH 4.5) when the Ub_2 chain is in the open conformation in solution, this suggests that the crystal conformation could be a result of the packing forces rather than a representative conformation at this pH. The solution structures at physiological conditions (Fig. 9b and c) reflect a dynamic equilibrium between the predominant, closed conformation and weakly populated, open conformation(s) of Ub_2 (see also below).

5.8. Independent validation of the closed conformation of Ub_2

The observed good agreement between the orientations obtained from two physically different methods, (1) measurements of the diffusion tensor and (2) measurements of molecular alignment in a liquid-crystalline medium, validates the closed conformation of Ub_2 described here. As an independent proof of the structural data, the observed Ub_2 conformation at neutral pH is in excellent agreement with the results of the intedomain interface mapping [13] based on the observed chemical shift perturbations between monoUb and Ub_2 (Fig. 10).

5.8.1. Site-directed spin labeling data support the closed conformation of Ub_2 at neutral pH

To further explore the observed closed conformation of Ub_2 we used site-directed spin labeling, which allowed us to identify residues that are close in space to a paramagnetic moiety covalently attached to a specific site on one of the domains. Paramagnetic relaxation probes enhance relaxation rates of nearby nuclei by a magnitude that depends on the electron–nuclear distance [77]:

$$\Delta R_{2para} = K[4\tau_c + 3\tau_c/(1 + \omega_H^2\tau_c^2)]/r^6. \tag{21}$$

Here R_{2para} is the increase in the ^{1}H transverse relaxation rate due to the presence of a paramagnetic spin S at a distance r from the nucleus and $K = (1/15)S(S + 1)\gamma_H^2 g_e^2 \beta_e^2$, where g_e is the electronic g-factor and β_e is the Bohr magneton. An almost three orders of magnitude stronger gyromagnetic ratio ($g_e\beta_e = 658\gamma_H\hbar$) for the electron spin makes it possible to obtain distance information of much longer range (up to ~ 25 Å) than that obtained through NOEs (up to ~ 5 Å).

The presence of a unique cysteine (Cys48) in the primary sequence of the K48C mutant used as the distal domain in Ub_2, allowed us to use a (1-oxyl-2,2,5,5-tetramethyl-3-pyrroline-3-methyl)methanesulfonate (MTSL) spin label that is highly specific for sulphydryl groups [78]. This molecule is also particularly appropriate because of the relatively small molar volume of its side chain. MTSL was

added to a protein sample from a concentrated stock in acetonitrile at a molar ratio of 3:1 MTSL:protein, and the mixture was incubated at room temperature for at least one hour. Excess MTSL reagent was removed by dialysis into NMR buffer. ^{1}H–^{15}N HSQC experiments were repeated after the spin-label was reduced with a threefold excess ascorbic acid, added in small volumes from a concentrated solution.

The nuclear–electron distances were obtained from the ratio of cross peak intensities in the ^{1}H–^{15}N HSQC spectra of the protein acquired with the spin label in the oxidized (paramagnetic) and in the reduced state, I_{ox} and I_{red}, respectively, using the following relationship [79]:

$$\Delta R_{2para} = R_{2ox} - R_{2red} = \ln(I_{ox}/I_{red})/t. \tag{22}$$

Here t denotes the total experimental time in which the amide proton magnetization is in the transverse plane and undergoing paramagnetic relaxation, and ΔR_{2para} is related to the inter-spin distance according to Eq. (21). The electron–nuclear distances derived from the intensity attenuations were then used as distance constraints to calculate the unpaired electron's position with respect to protein coordinates via an optimization search implemented in an in-house Matlab program.

Spin-labeling of Ub_1 (K48C) was performed as a control and for distance calibration purposes. The pattern of intensity attenuations observed in the HSQC spectra at pH 6.8 clearly identifies a region of perturbed residues around the position of C48. Residues L43–Q62 experience intensity attenuations greater than 20%, while the largest effect (more than 80% attenuation) was observed in residues F45–E51 (adjacent to C48) and D58–Q62 (close in space to C48). Converting these attenuations into distance constraints, the position of the unpaired electron was found to be at a distance of about 4.5 Å from the beta-carbon of C48, which appears reasonable considering the size of the modified residue and reorientational dynamics of the spin label. The results obtained at pH 4.5 are practically identical.

The same experiments were then performed on Ub_2, where MTSL was covalently attached to C48 in the distal domain. Two different Ub_2 samples were used, having only one of the two domains ^{15}N-labeled. The attenuation pattern for the distal domain was very similar to that of monoUb, although the magnitude of the effect was generally stronger, consistent with the increased molecular weight (hence slower tumbling) of the molecule. Furthermore, some attenuation was observed around I23. These observations can be explained by increased τ_c (Ub_2 versus Ub_1) that makes paramagnetic enhancement effect stronger and extends it to greater distances from the spin label. Finally, a relaxation enhancement was observed in some residues at the C-terminus of Ub_2-D, probably because they get closer to C48 in Ub_2, as a result of the linkage between the domains. The reconstructed position of the spin label's electron was at a distance of 3.5 Å from the beta-carbon of
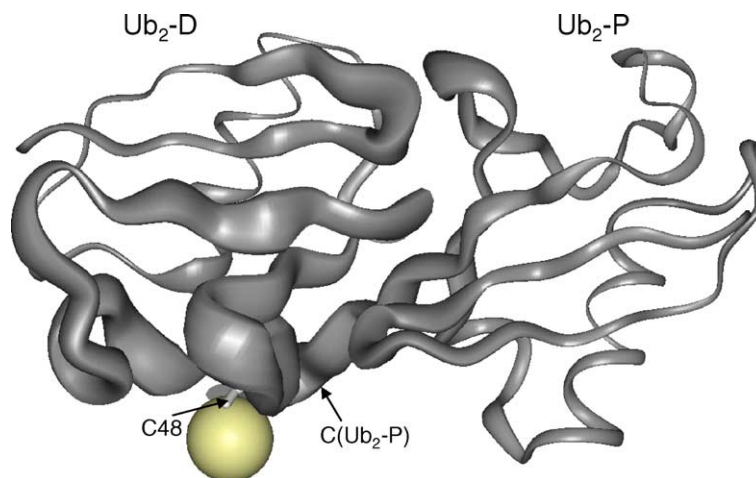
Fig. 11. Validation of the closed conformation of Ub$_2$ using site-directed spin labeling. Shown is the Ub$_2$ conformation derived from RDC measurements (Figs. 9c and 10), with the ribbon width proportional to relaxation rate enhancement caused by MTSL attached to C48 (indicated) in the distal domain. Also shown is the location of the unpaired electron (sphere) reconstructed from the observed signal attenuation in the distal domain (left), as well as the location of C48 (stick). The orientation of the molecule is similar to that in Fig. 10. The domains were positioned closer to each other than in Fig. 10 by translating them along the z-axis of Ub$_2$.

C48 (Fig. 11), which is similar to that found for monoUb. The results at pH 4.5 were practically the same, although less attenuation was observed around I23.

Most interesting are paramagnetic relaxation enhancements in the proximal domain when the spin-label was attached to C48 in the distal Ub. The attenuations here were up to about 70% and overall somewhat weaker than in the distal domain itself. The major relaxation rates enhancements were observed for residues T7–T12 and H68–G76 (including C-terminus of Ub$_2$-P) that are facing C48 on the distal domain (Fig. 11) in the solution structures of Ub$_2$ determined here. In addition, attenuation was observed in some residues around R42 and K48 located at the interdomain interface. These data by themselves confirm the existence of the closed conformation of Ub$_2$ and agree with the relative orientation of the two domains determined here.

Using the attenuations observed in the proximal Ub, we have calculated the position of the spin label's unpaired electron relative to this domain. We have also attempted to use this information to determine the interdomain distance, which is not available from the orientational constraints, as discussed above. By starting with the RDC-derived solution structure of Ub$_2$ (Fig. 9c) and translating the two domains closer to one another along the z-axis, we were able to bring the position of the spin label 'seen' by the proximal domain reasonably close (9.3 Å from C$_\beta$ of C48) to its position determined based on the distal domain data. Differences in these positions can be ascribed to the equilibrium dynamics between open and closed conformations of Ub$_2$ and to the intrinsic flexibility of the spin label. These results further support the above-determined interdomain orientation in Ub$_2$ at neutral pH. Accurate refinement of the Ub$_2$ structure based on these data would require protein docking

approaches [26,27] using a combination of the orientational and distance (spin label) constraints, together with the chemical shift perturbation mapping. The same residues in Ub$_2$-P (T7–T12, H68–G76) showed signal attenuation at pH 4.5, although with a significantly lesser magnitude of the effect, consistent with a shift in the equilibrium towards the open conformation(s) of Ub$_2$.

6. Dynamics of di-ubiquitin

6.1. Amplitudes of intradomain backbone dynamics are similar in Ub$_2$ and monoUb

As indicated above, the derivation of the diffusion tensor, Eqs (11)–(15), assumes that local backbone dynamics in Ub$_2$ are restricted and uncoupled from the overall motion, hence they do not affect the experimental values of ρ. In order to verify that the obtained diffusion tensors are not biased by these assumptions, we calculated order parameters [80] for the backbone amides in each Ub domain in Ub$_2$ and compared them with those for monoUb. The underlying assumption is that local subnanosecond dynamics should not depend on whether Ub is in monomeric state or is included in Ub$_2$. The comparison of the order parameters (Fig. 12) shows an excellent agreement of the pictures of the local dynamics in Ub in both states. The main difference is observed in the C-terminus of the distal domain, which is free and flexible in monoUb but shows restricted mobility in Ub$_2$ because of its chemical link to K48 of the proximal domain. Consistent with this, smaller amplitudes of backbone dynamics are also observed around K48 in the proximal domain. β1/β2 loops in both domains are located at the interdomain interface in Ub$_2$ and
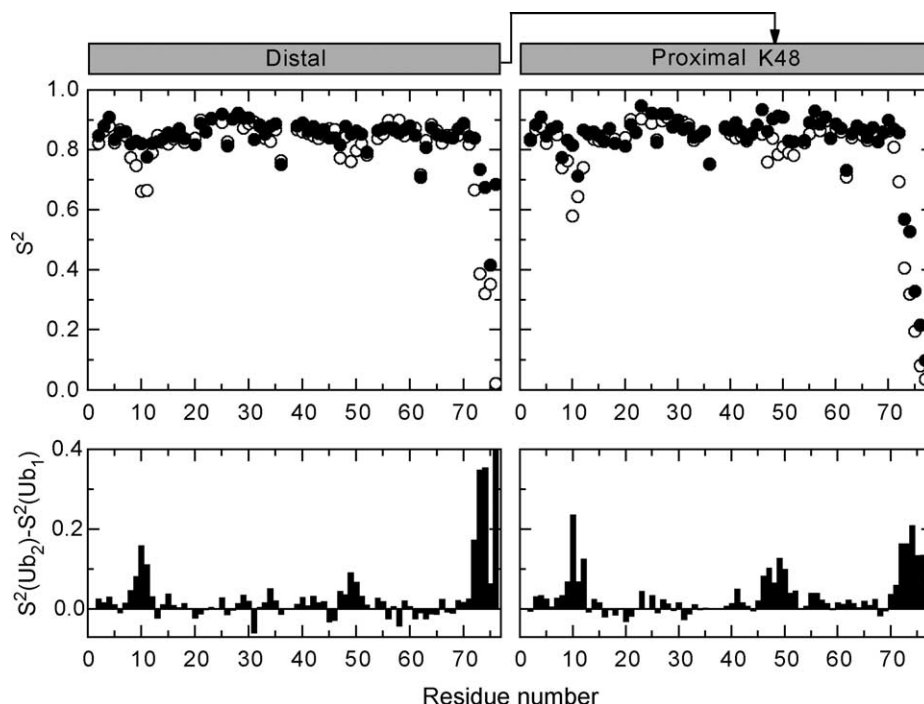
Fig. 12. Comparison of the order parameters representing local backbone dynamics in Ub_2 (solid circles) and in monoUb (open circles) indicates that local motions are not affected by the formation of Ub_2. The model-free parameters were derived from analysis of ^{15}N relaxation data using computer program DYNAMICS [67,84] and taking into account rotational anisotropy of Ub_2 (Table 3) and monoUb (data not shown).

therefore are somewhat more restricted than in monoUb. Also the C-terminus of the proximal domain appears less flexible than in monoUb, which could be caused by its positioning close to the distal domain.

6.2. Interdomain dynamics in Ub_2

6.2.1. The interdomain interface in Ub_2 is dynamic

Although Ub_2 at neutral pH is characterized by a well-defined interface between Ub domains, this conformation is not locked. Indeed, our studies of Ub_2 binding to various ligands suggest that the interdomain interface could be accessible for interactions with other molecules. For example, solvent accessibility studies [13] using a soluble paramagnetic relaxation agent HyTEMPO (4-hydroxy-2,2,6,6-tetramethylpiperidinyl-1-oxy) showed that this nitroxyl radical can get access to residues buried in the interdomain interface in Ub_2. Moreover, the data suggest that HyTEMPO gets transiently trapped in the hydrophobic interface. Consistent with the finding that Ub_2 is in equilibrium between the closed and open conformations, these data indicate that the amplitudes of the interdomain motions could be sufficient to open the interface, so that the functionally important residues L8, I44, and V70 located at the Ub_2 interface become available for interactions with other molecules.

The presence of interdomain mobility in Ub_2 is also consistent with the fact that the observed anisotropy of the diffusion tensor ($\xi \sim 1.2–1.5$, Table 3) is markedly smaller than that expected for an ellipsoid of revolution with a 2:1

axial ratio ($\xi = 1.87$ [81]) or for a system of two rigidly attached spheres with no hydration shell ($\xi = 2.3$ [60]). The reduced apparent anisotropy of the tensor is the result of its averaging by the interdomain dynamics. Interestingly, both the diffusion and the alignment tensors experienced by the distal Ub appear more axially symmetric than those for the proximal domain. This asymmetry between the two domains most likely reflects the asymmetric nature of their linkage, which could result in differential averaging of the individual components of the tensors for the two domains.

6.2.2. How fast are the interdomain motions in Ub_2?

The dynamic character of the Ub_2 conformation at neutral pH is further supported by the conformational exchange broadening observed in several residues located at the interface in Ub_2. (Table 5, Fig. 11) This is indicative of conformational exchange-type motions in the microsecond-millisecond time scale. Most of these conformational exchange contributions are absent in the data measured at pH 4.5, indicating that these motions are specific to Ub_2 conformation at neutral pH. It seems natural to assume that this is a result of an exchange between a closed conformation and one or more open conformations. Given a single peak is observed per residue, we assume that this exchange is in the fast regime on the NMR time scale. From the observed R_{ex} contributions to R_2 values we estimated the characteristic time of these processes using the following

Table 5
The characteristic time constants for conformational exchange motions in Ub_2

Residue[a]	R_{ex},[b] s^{-1}	$\Delta\delta(^{15}N)$, ppm[c]	τ_{ex},[d] μs
Distal			
Q2	0.62 ± 0.14	0.26	497 ± 306
V5	0.46 ± 0.20	0.39	166 ± 103
T7	1.22 ± 0.18	−0.97	70 ± 24
Q41	0.61 ± 0.23	−0.39	216 ± 126
K48	0.81 ± 0.18	−0.91	53 ± 20
H68	0.52 ± 0.16	−0.58	83 ± 39
V70	2.58 ± 1.56	−0.97	148 ± 100
Proximal			
T7	1.06 ± 0.16	−0.97	61 ± 21
Q41	0.75 ± 0.17	−0.39	271 ± 132
R42	1.20 ± 0.32	−0.39	429 ± 217
K48	1.21 ± 0.21	−0.26	973 ± 582
E51	1.19 ± 0.35	−0.52	240 ± 113
Y59	0.40 ± 0.10	−0.19	564 ± 433
H68	1.42 ± 0.33	−0.58	225 ± 96
V70	2.08 ± 0.51	−1.10	93 ± 36
R72	1.34 ± 0.24	−0.26	1070 ± 641

[a] Only residues with noticeable ^{15}N chemical shift difference between Ub_2 and monoUb are shown here. Data for I23 are not included, because this residue shows strong exchange broadening already in monoUb [52].

[b] Conformational exchange contributions to ^{15}N R_2 determined from model-free analysis of the relaxation data using computer program DYNAMICS [67,84].

[c] The maximal ^{15}N chemical shift difference between Ub_2 and monoUb observed in the course of pH titration.

[d] Characteristic time constants for conformational exchange motions were determined using Eq. (23). Note that these numbers provide an upper-limit estimate for τ_{ex}, because (1) the chemical shift differences between the closed and open states of Ub_2 could be underestimated and (2) some of these residues (e.g. Q2 and V70) show weak exchange broadening already in monoUb.

equation:

$$\tau_{ex} = \frac{R_{ex}}{p_{op}p_{cl}(\Delta\omega)^2}. \tag{23}$$

Here p_{op} and p_{cl} are the fractional populations of the open and closed states (taken as 0.15 and 0.85, respectively, at pH 6.8), and the frequency difference, $\Delta\omega$, between the two exchanging states was estimated from the maximal ^{15}N chemical shift difference between monoUb and Ub_2 observed for a given residue in the course of pH titration.

The derived values of τ_{ex} (Table 5) range from 50 μs up to ~ 1 ms. The fastest exchange rates were observed for K48 and H68 in the distal domain, V70 in the proximal, and for T7 in both domains, all located at the interdomain interface (Fig. 11). The location of the sites showing exchange broadening at or close to the interface suggests that the observed conformational exchange is caused by the equilibrium dynamics between the closed and open conformations of Ub_2. These data provide an estimate of the time scale for the opening/closing motions and thus complement the TEMPO-accessibility data that indicate noticeable amplitudes of these motions.

7. Some issues to be aware of

7.1. Interdomain mobility

The concept of a common tensor requires a certain correlation in the tumbling or orientation between the domains, so that they behave as a single entity. In reality, components of a multidomain system are rarely (if at all) locked in one particular conformation, so some interdomain mobility is always present. It is obvious that the domain orientation approach described here is not applicable to those multidomain systems where individual domains reorient independently, i.e. behave like 'independent beads on a flexible string'. Therefore the applicability of this approach to a particular protein system requires validation.

Note also that the methods described here provide a time-averaged information on interdomain orientation. Differential averaging of the structural information by RDC and relaxation measurements in the presence of interdomain motions could result in differences in the domain orientation derived by the two methods. This effect will depend on a particular mechanism of interdomain mobility (e.g. twisting, bending, or stretching) and on the characteristic time scales of these motions that could vary from one molecular system to another. Note that spin-relaxation rates are primarily sensitive to inter- and intradomain dynamics that are faster than the overall tumbling (i.e. from picoseconds to nanoseconds) whereas the measured RDCs are affected by a much broader range of motions, from picoseconds up to milliseconds and slower.

7.2. Structures of individual domains

The knowledge of the 3D structure for each domain is essential for the domain orientation approach described here. In the case illustrated here, we have used a known solution structure of ubiquitin in the monomeric state, and assumed that there is no change in the local structure of the individual domains when they form Ub_2. This is fully justified here by (1) the relatively small magnitude of the chemical shift perturbations compared to monoUb (Figs. 1 and 2) by the excellent agreement between the experimental RDC values and those back-calculated using the structure of monoUb (Fig. 8). Note also that similar characteristics of the diffusion and alignment tensors were obtained [13] when using individual domain structures observed in the crystals of Ub_2 or Ub. When the structures of the individual domains are significantly perturbed in the context of a multidomain system, e.g. as a result of tight binding, their actual structure in the complex must be determined prior to applying the domain orientation methods discussed above. In this case it might prove useful to include the diffusion- or alignment-derived information in the form of orientational constraints directly into the structure refinement steps.
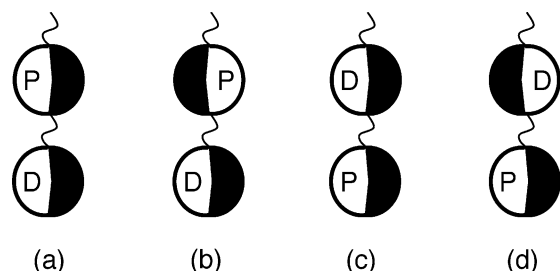
Fig. 13. Illustration of the degeneracy of possible solutions for the interdomain orientation determined from the PAFs of the diffusion or alignment tensors. Because these tensors are not sensitive to the directionality (sign) of the axes, all four interdomain orientations schematically shown here are consistent with measured tensor orientations. The degeneracy could be removed by adding specific information, e.g. on the nature of the chemical linkage between the domains, domain-specific chemical shift perturbations, NOE contacts, etc.

7.3. Orientational degeneracy

Neither diffusion nor alignment tensors have directionality, i.e. they cannot distinguish between x and $-x$, z and $-z$, etc. Therefore, the derived tensor orientation has a fourfold degeneracy, as the sets of Euler angles $\{\alpha, \beta, \gamma\}$, $\{\alpha, \beta, \gamma + 180°\}$, $\{\alpha + 180°, 180° - \beta, 180° - \gamma\}$, and $\{\alpha + 180°, 180° - \beta, 360° - \gamma\}$ are all equivalent [2]. As a result, the total number of possible domain orientations in the 3D space is 16 for a dual-domain system [49]. Of these, only four represent different interdomain orientations, which would correspond to having orientation of one of the two domains fixed and allowing the other domain to adopt all possible orientations consistent with the data (Fig. 13). The degeneracy could be further reduced if additional considerations specific for a particular molecular system can be applied. For example, the conformations shown in Fig. 13c and d can be ruled out because of a specific direction of the chemical linkage between the distal and the proximal Ub domains in Ub$_2$. Of the remaining two conformations, one was inconsistent with specific chemical shift perturbations observed in the Ub units upon Ub$_2$ formation and with our spin-labeling data.

7.4. Orientational sampling

The accuracy of the tensor determination strongly depends on the amount of available experimental data: one needs at least six independent measurements/vectors for the diffusion tensor and five for the alignment tensor. It is critical that the orientational information is obtained from 'independent' measurements, i.e. that the experimentally observed set of NH (or other) vectors samples the orientational space uniformly. Otherwise, the derived tensor parameters could be biased if some orientations are underrepresented, i.e. are not sampled properly. For example, having several parallel vectors (as e.g. NH vectors in the α-helix) does not provide new information compared to just one of them. This issue could be

particularly important for measurements using NH vectors, which represent the worst sampling set of backbone internuclear bond vectors in proteins [59]. The problem of orientational sampling has been addressed in Ref. [59]. The set of NH vectors in each Ub domain used in this study is characterized by the generalized sampling parameter of 0.12, which provides a reasonable sampling of the orientational space.

8. Concluding remarks

Here we discussed two NMR methods for determining interdomain orientation based on long-range, internuclear vector constraints arising from the anisotropy of molecular tumbling or molecular orientations in solution. These approaches could become a method of choice for structure characterization of multidomain proteins or protein complexes with relatively weak interactions between the individual, well-structured components, as these systems might not be suitable for crystallography or conventional, NOE-based NMR approaches. We illustrated these methods by determining the relative orientation of ubiquitin units in K48-linked di-ubiquitin at acidic and neutral pH. The derived structures represent two distinct conformations of the chain: an open one at pH 4.5 and a predominantly closed conformation at physiological conditions. In the latter case, the interdomain interface is well defined and is formed by the hydrophobic patches (comprising L8–I44–V70) on both Ub domains. These data are also supported by the results of chemical shift mapping of the interface and by site-directed spin labeling. Our studies show that the functionally important residues L8, I44, and V70 located at the Ub$_2$ interface are not rigidly buried and that the interdomain dynamics could be sufficient to allow these groups to interact with other molecules. This also suggests that the interdomain mobility could play an important regulatory role in the function of polyUb chains, by allowing the functionally important hydrophobic residues (sequestered at the interface between Ub domains) to interact with recognition factors that could compete with the Ub–Ub interaction.

We have also discussed in detail the process of determining the rotational diffusion tensor of a molecule from ^{15}N relaxation data. An extensive analysis of computer-generated relaxation data allowed us to explore the characteristic features of fully anisotropic tumbling and to address the issues of precision and accuracy of the tensor determination from experimental data.

References

[1] F. Sicheri, J. Kuriyan, Curr. Opin. Struct. Biol. 7 (1997) 777–785.

[2] R. Bruschweiler, X. Liao, P.E. Wright, Science 268 (1995) 886–889.

[3] N. Tjandra, S.E. Feller, R.W. Pastor, A. Bax, J. Am. Chem. Soc. 117 (1995) 12562–12566.

[4] D. Fushman, D. Cowburn, Studying protein dynamics with NMR relaxation, in: R. Sarma, M. Sarma (Eds.), Structure, Motion, Interaction and Expression of Biological Macromolecules, Adenine Press, Albany, NY, 1998, pp. 63–77.

[5] J.R. Tolman, J.M. Flanagan, M.A. Kennedy, J.H. Prestegard, Proc. Natl Acad. Sci. USA 92 (1995) 9279–9283.

[6] N. Tjandra, A. Bax, Science 278 (1997) 1111–1114.

[7] D. Fushman, R. Xu, D. Cowburn, Biochemistry 38 (1999) 10225–10230.

[8] M.W.F. Fischer, J.A. Losonczi, L.J. Weaver, J.H. Prestegard, Biochemistry 38 (1999) 9013–9022.

[9] N. Skrynnikov, N. Goto, D. Yang, W. Choy, J. Tolman, G. Mueller, L. Kay, J. Mol. Biol. 295 (2000) 1265–1273.

[10] P.M. Hwang, N.R. Skrynnikov, L.E. Kay, J. Biomol. NMR 20 (2001) 83–88.

[11] J. Evenas, V. Tugarinov, N.R. Skrynnikov, N.K. Goto, R. Muhandiram, L.E. Kay, J. Mol. Biol. 309 (2001) 961–974.

[12] T.S. Ulmer, J.M. Werner, I.D. Campbell, Structure (Camb) 10 (2002) 901–911.

[13] R. Varadan, O. Walker, C. Pickart, D. Fushman, J. Mol. Biol. 324 (2002) 637–647.

[14] V. Tugarinov, L.E. Kay, J. Mol. Biol. 327 (2003) 1121–1133.

[15] R. Varadan, M. Assfalg, A. Haririnia, S. Raasi, C. Pickart, D. Fushman, J. Biol. Chem. 279 (2004) 7055–7063.

[16] A. Hershko, A. Ciechanover, Annu. Rev. Biochem. 67 (1998) 425–480.

[17] L. Hicke, R. Dunn, Annu. Rev. Cell Dev. Biol. 19 (2003) 141–172.

[18] C.M. Pickart, Annu. Rev. Biochem. 70 (2001) 503–533.

[19] V. Chau, J.W. Tobias, A. Bachmair, D. Marriott, D.J. Ecker, D.K. Gonda, A. Varshavsky, Science 243 (1989) 1576–1583.

[20] D. Finley, S. Sadis, B.P. Monia, P. Boucher, D.J. Ecker, S.T. Crooke, V. Chau, Mol. Cell Biol. 14 (1994) 5501–5509.

[21] J.S. Thrower, L. Hoffman, M. Rechtenstein, C.M. Pickart, EMBO J. 19 (2000) 94–102.

[22] W.J. Cook, L.C. Jeffrey, M. Carson, C. Zhijian, C.M. Pickart, J. Biol. Chem. 267 (1992) 16467–16471.

[23] W.J. Cook, L.C. Jeffrey, E. Kasperek, C.M. Pickart, J. Mol. Biol. 236 (1994) 601–609.

[24] C.L. Phillips, J. Thrower, C.M. Pickart, C.P. Hill, Acta Crystallogr. D 57 (2000) 341–344.

[25] G.M. Clore, A.M. Gronenborn, Proc. Natl Acad. Sci. USA 95 (1998) 5891–5898.

[26] G.M. Clore, Proc. Natl Acad. Sci. USA 97 (2000) 9021–9025.

[27] C. Dominguez, R. Boelens, A.M. Bonvin, J. Am. Chem. Soc. 125 (2003) 1731–1737.

[28] J. Meiler, N. Blomberg, M. Nilges, C. Griesinger, J. Biomol. NMR 16 (2000) 245–252.

[29] H. Goldstein, Classical Mechanics, second ed., Addison-Wesley, Reading, MA, 1980.

[30] R. Tycko, F.J. Blanco, Y. Ishii, J. Am. Chem. Soc. 122 (2000) 9340–9341.

[31] S. Meier, D. Haussinger, S. Grzesiek, J. Biomol. NMR 24 (2002) 351–356.

[32] S. Grzesiek, A. Bax, J.S. Hu, J. Kaufman, I. Palmer, S.J. Stahl, N. Tjandra, P.T. Wingfield, Protein Sci. 6 (1997) 1248–1263.

[33] B.F. Volkman, S.J. Wilkens, A.L. Lee, B. Xia, W.M. Westler, R. Beger, J.L. Markley, J. Am. Chem. Soc. 121 (1999) 4677–4683.

[34] H. Demene, P. Tsan, P. Gans, D. Marion, J. Phys. Chem. B 104 (2000) 2559–2569.

[35] L. Banci, I. Bertini, J.G. Huber, C. Luchinat, A. Rosato, J. Am. Chem. Soc. 120 (1998) 12903–12909.

[36] E. de Alba, J.L. Baber, N. Tjandra, J. Am. Chem. Soc. 121 (1999) 4282–4283.

[37] M. Zweckstetter, A. Bax, J. Am. Chem. Soc. 122 (2000) 3791–3792.

[38] A. Bax, G. Kontaxis, N. Tjandra, Meth. Enzymol. 339 (2001) 127–174.

[39] J.R. Tolman, Curr. Opin. Struct. Biol. 11 (2001) 532–539.

[40] F. Tian, H.M. Al-Hashimi, J.L. Craighead, J.H. Prestegard, J. Am. Chem. Soc. 123 (2001) 485–492.

[41] P.J. Bolon, H.M. Al-Hashimi, J.H. Prestegard, J. Mol. Biol. 293 (1999) 107–115.

[42] B.W. Koenig, D.C. Mitchell, S. Konig, S. Grzesiek, B.J. Litman, A. Bax, J. Biomol. NMR 16 (2000) 121–125.

[43] A. Saupe, Angew Chem. Int. Ed. 7 (1968) 97–112.

[44] J.R. Tolman, H.M. Al-Hashimi, L.E. Kay, J.H. Prestegard, J. Am. Chem. Soc. 123 (2001) 1416–1424.

[45] J.A. Losonczi, M. Andrec, M.W. Fischer, J.H. Prestegard, J. Magn. Reson. 138 (1999) 334–342.

[46] W.H. Press, S.A. Teukolsky, W.T. Vetterling, B.P. Flannery, Numerical Recipes in C, Cambridge University Press, Cambridge, 1992.

[47] L.K. Lee, M. Rance, W.J. Chazin, A.G. Palmer III, J. Biomol. NMR 9 (1997) 287–298.

[48] V. Copie, Y. Tomita, S.K. Akiyama, S. Aota, K.M. Yamada, R.M. Venable, R.W. Pastor, S. Krueger, D.A. Torchia, J. Mol. Biol. 277 (1998) 663–682.

[49] R. Ghose, D. Fushman, D. Cowburn, J. Magn. Reson. 149 (2001) 214–217.

[50] D. Fushman, D. Cowburn, Characterization of inter-domain orientations in solution using the NMR relaxation approach, in: N.R. Krishna, L.Berlines (Eds.), Protein NMR for the Millenium, Biological Magnetic Resonance, vol. 20, Kluwer, Dordrecht, 2002, pp. 53–78.

[51] D. Fushman, N. Tjandra, D. Cowburn, J. Am. Chem. Soc. 120 (1998) 10947–10952.

[52] D. Fushman, N. Tjandra, D. Cowburn, J. Am. Chem. Soc. 121 (1999) 8577–8582.

[53] D. Woessner, J. Chem. Phys. 37 (1962) 647–654.

[54] D. Fushman, Determination of protein dynamics using ^{15}N relaxation measurements, in: O. Zerbe (Ed.), BioNMR in Drug Research, Wiley–VCH, New York, 2002, pp. 283–308.

[55] P. Dosset, J.C. Hus, M. Blackledge, D. Marion, J. Biomol. NMR 16 (2000) 23–28.

[56] D. Fushman, T. Najmabadi-Haske, S. Cahill, J. Zheng, H. LeVine, 3rd, D. Cowburn, J. Biol. Chem. 273 (1998) 2835–2843.

[57] P.R. Bevington, D.K. Robinson, Data Reduction and Error Analysis for the Physical Sciences, second ed., McGraw-Hill, New York, 1992, pp. 205–209.

[58] G.M. Clore, D.S. Garrett, J. Am. Chem. Soc. 121 (1999) 9008–9012.

[59] D. Fushman, R. Ghose, D. Cowburn, J. Am. Chem. Soc. 122 (2000) 10640–10649.

[60] J.M. Schurr, H.P. Babcock, B.S. Fujimoto, J. Magn. Reson. B105 (1994) 211–224.

[61] J. García de la Torre, M.L. Huertas, B. Carrasco, J. Magn. Reson. B147 (2000) 138–146.

[62] M. Blackledge, F. Cordier, P. Dosset, D. Marion, J. Am. Chem. Soc. 120 (1998) 4538–4539.

[63] R. Xu, B. Ayers, D. Cowburn, T.W. Muir, Proc. Natl Acad. Sci. USA 96 (1999) 388–393.

[64] J. Piotrowski, R. Beal, L. Hoffmann, K.D. Wilkinson, R.E. Cohen, C.M. Pickart, J. Biol. Chem. 272 (1997) 23712–23721.

[65] D. Fushman, S. Cahill, D. Cowburn, J. Mol. Biol. 266 (1997) 173–194.

[66] J.A. Jones, J. Magn. Res. 126 (1997) 283–286.

[67] J.B. Hall, D. Fushman, J. Biomol. NMR 27 (2003) 261–275.

[68] N. Tjandra, A. Bax, Science 278 (1997) 1111–1114.

[69] M. Ruckert, G. Otting, J. Am. Chem. Soc. 122 (2000) 7793–7797.

[70] M. Ottiger, F. Delaglio, A. Bax, J. Magn. Reson. 131 (1998) 373–378.

[71] D.S. Garrett, R. Powers, A.M. Gronenborn, G.M. Clore, J. Magn. Reson. 95 (1991) 214–220.

[72] R.M. Hofmann, C.M. Pickart, Cell 96 (1999) 645–653.

[73] J. Spence, S. Sadis, A. Haas, D. Finley, Mol. Cell Biol. 15 (1995) 1265–1273.

[74] L. Deng, C. Wang, E. Spencer, L. Yang, A. Braun, J. You, C. Slaughter, C. Pickart, Z.J. Chen, Cell 103 (2000) 351–361.

[75] J. Spence, R.R. Gali, G. Dittmar, F. Sherman, M. Karin, D. Finley, Cell 102 (2000) 67–76.

[76] J.M. Galan, R. Haguenauer-Tsapis, EMBO J. 16 (1997) 5847–5854.

[77] P.A. Kosen, Meth. Enzymol. 177 (1989) 86–121.

[78] L.J. Berliner, J. Grunwald, H.O. Hankovszky, K. Hideg, Anal. Biochem. 119 (1982) 450–455.

[79] N.U. Jain, A. Venot, K. Umemoto, H. Leffler, J.H. Prestegard, Protein Sci. 10 (2001) 2393–2400.

[80] G. Lipari, A. Szabo, J. Am. Chem. Soc. 104 (1982) 4546–4559.

[81] S. Koenig, Biopolymers 14 (1975) 2421–2423.

[82] R. Koradi, M. Billeter, K. Wuthrich, J. Mol. Graph. 14 (1996) 51–55.

[83] G. Cornilescu, J.L. Marquardt, M. Ottiger, A. Bax, J. Am. Chem. Soc. 120 (1998) 6836–6837.

[84] D. Fushman, S. Cahill, D. Cowburn, J. Mol. Biol. 266 (1997) 173–194.